POLITECNICO DI TORINO

Master's Degree in Nanotechnologies for ICTs

Master's Degree Thesis

Modeling of Weyl semimetal devices

Supervisors:

Dr. Alberto TIBALDI

Prof. Francesco BERTAZZI

Prof. Michele GOANO

External tutor: Dr. Cezar ZOTA

Candidate:

Lorenzo ROCCHINO

October, 2020

"In my work I always try to combine beauty with truth,
but when I have to choose between one or the other, I generally choose beauty"

Hermann Weyl

Abstract

The main goal of this work is to develop a robust device modeling framework encompassing the unique physics found in Weyl semimetals, and to use this framework to design and simulate the behaviour of new electrical devices. Weyl semimetals, due to their unusual band structure (which is gapped except at some isolated points, called Weyl nodes) have been shown to exhibit interesting properties such as a huge magneto-resistance at cryogenic temperatures, and a set of different transport mechanisms that arise from a unique phenomena called chiral anomaly. Applications-wise, the focus of this work is on two possible device implementations: a Weyl semimetal amplifier and an oscillator. These two device concepts are designed to work under low power and cryogenic conditions, which make them highly suitable for quantum-computing applications.

Concerning the oscillator, the work mainly focuses on the possibility of achieving a coherent output field generation and the description of the working conditions that are needed to fulfill that goal. The main components of the device concept are a Weyl semimetal slab, coupled with a charge sensing device. The Weyl semimetal slab is subjected to crossed magnetic and electric field: this condition is able to produce an exotic trajectory for the electrons inside the slab, that translates into the generation of an oscillating electric field. The charge sensing device, in its simplest configuration, can be simply a standard transistor or, even better, a quantum dot. The work on the amplifier is based on a device model consisting of a superconductive gating of a Weyl semimetal channel, and focuses on the understanding and modelling of the underlying physics, in order to have a clear perspective of its performance, compared to the existing competing technologies.

Most of the modeling work was performed within the MATLAB environment: for specific simulations, such as the FEM solution of the 3D London equation for the supercurrent density profile in the gate of the Weyl semimetal amplifier, ad-hoc tools have been used.

Acknowledgements

I would like to spend few words to thank all the people who collaborated in the realization of this work.

First, I thank my supervisors, Dr. Alberto Tibaldi, Prof. Francesco Bertazzi and Prof. Michele Goano, for agreeing to help me and for their guidance and support in tackling this thesis project.

I sincerely thank my external supervisor, Dr. Cezar Zota, for all the work done together in the past months: I could not have wished for a more kind, helpful and knowledgeable person. With him, I also take the opportunity to thank all the MIND group at IBM Research, for the cordiality and support shown to me during my staying.

I obviously thank my family, my parents, for supporting me over the years and for accepting and encouraging my every decision: I know how difficult it may have been for you to let me go, even if it was only for a short time. I thank you for that.

I thank my university colleagues for sharing this important period of my life with me: I feel like I have received more than I have given you, and I can only be grateful for this.

Finally, I warmly thank all the friends who accompanied me along this journey, to those who were there from the beginning and to those who joined along the way. I feel extremely lucky to be able to share this milestone with you. Because after all, whatever you do in this life, it's not worth, unless your friends are there to see it.

To all of you, thank you!

Table of Contents

Acronyms

ALD
: Atomic layer deposition

BS
: Biot-Savart

CMEF
: Crossed magnetic and electric fields

CMOS
: Complementary metal-oxide-semiconductor

DSM
: Dirac semimetal

FS
: Fermi surface

HEMT
: High-electron-mobility transistor

LL
: Landau level

MR
: Magnetoresistance

NMR
: Negative magnetoresistance

RF

Radio frequency

SdH

Shubnikov-de Haas

SC

Superconductor

SOC

Spin-orbit coupling

TI

Topological insulator

VCO

Voltage-controlled oscillator

WSA

Weyl semimetal amplifier

WSM

Weyl semimetal

WSO

Weyl semimetal oscillator

List of Figures

List of Tables

Chapter 1

Introduction

1.1 Brief history of Weyl semimetals

In 1929, the German mathematician Hermann Weyl came up with a simplification of the recently proposed Dirac equation, which was the first successful attempt to reconcile quantum mechanics with Einstein theory of special relativity. The Weyl equation, in its general form, has the following expression [1]:

$$\sigma^{\mu}\partial_{\mu}\psi = 0 \tag{1.1}$$

This equation describes relativistic massless fermions with a defined chirality. For more than 80 years, neutrinos where believed to be Weyl fermions: it was only in 2015 that the Nobel laureates Takaaki Kajita and Arthur McDonald demonstrated that neutrinos have mass [2]. Currently there are no fundamentals particle that can embody the concept of Weyl fermions [3]. They are instead conceived as quasi-particles associated to low-energy excitations that can carry electrical charge in some specific solid crystals: this class of topological materials is called Weyl semimetals.

The first experimentally discovered WSM was TaAs, by angle-resolved photoemission spectroscopy, in 2015 [4]. At the moment there are several other families of materials that have been reported to carry Weyl fermions, such as Cd_3As_2, CoSi, $MoTe_2$, NbP, TaP, WP_2 and other more [5][6][7].

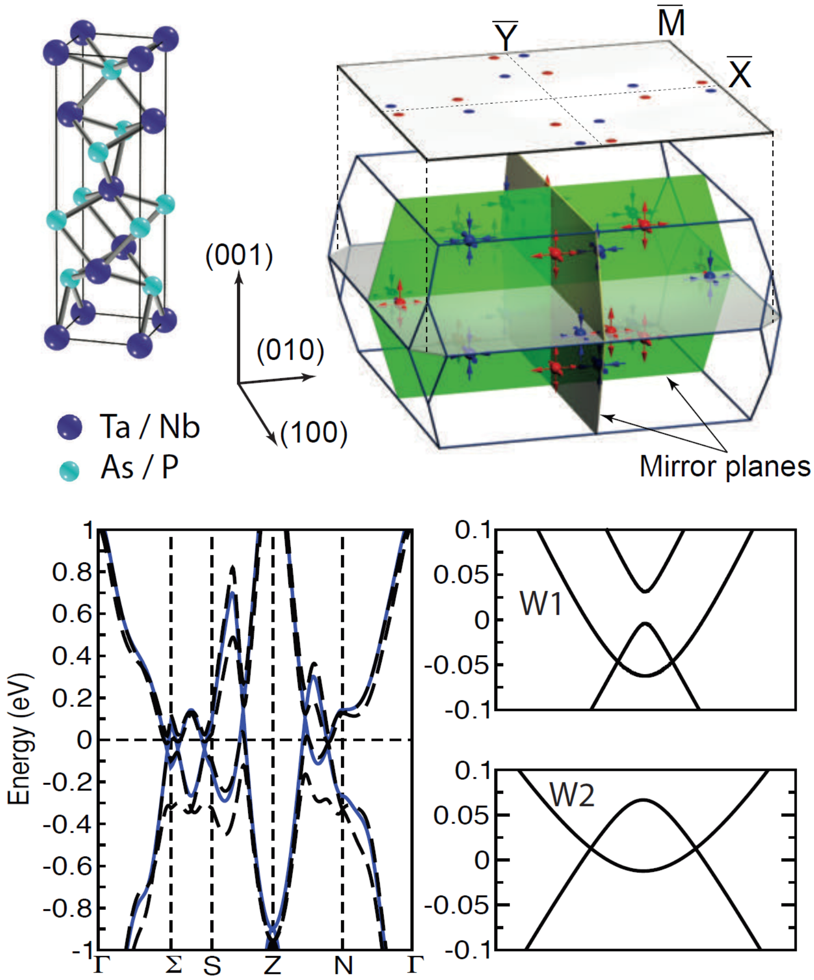

Figure 1.1: Crystal structure and bulk band structure of the WSM family of TaAs compound (top panels). The bottom panels report the bulk band structure along some high symmetry lines (with and without SOC) on the left and the energy dispersion across a pair of Weyl points in the right panels. Taken from [8].

1.2 Topological phases of matter

The different properties of materials are supposed to come from the different ways in which atoms are organized; however, the standard classification into solid, liquid and gas is too simplistic to explain some particular phenomena that arise in nature. A more advanced classification was proposed by Lev Landau [9]: his symmetry-breaking theory provides a general understanding of the different phases in which materials organize themselves. He pointed out that, as a material undergoes a phase transition, the symmetry of the organization of atoms changes and that transition can be described by means of an order parameter [10]. Landau symmetry-breaking theory has been believed for a long time to be capable of describing all possible orders in materials, and all possible phase transitions, but it is still incomplete. There are in fact materials which have the same symmetry, but are distinct because of topology: a classic example are the so-called topological insulators [11]. Topology is a mathematical concept that is adapted to describe to the fact that certain materials properties remain invariant under continuous deformation such as stretching, bending or twisting.

1.2.1 Topological insulators

Classical insulators are materials in which the ensembles of valence bands are separated from the conduction bands by an energy gap near the Fermi level. Topological insulators instead have a non-trivial topology of the bands, i.e not all insulating phases are equal to each other. The presence of topological order in insulating materials leads to characteristic effects, the most relevant is the existence of gapless surface states [11]. Despite the energy gap in the band structure, the surface of a topological insulator has a metallic behaviour [11] (Fig. 1.2).

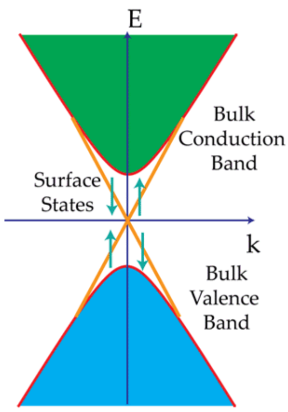

Figure 1.2: Band structure of a topological insulator: the Fermi level lies within the band gap, which is traversed by topologically-protected surface states.

These surface states, though, are not exactly like any other surface state: they are said to be topologically protected, which means that they are robust against any local perturbations that can break all the symmetries [12].

1.2.2 Weyl and Dirac semimetals

The materials that show this peculiar topology are found to be materials with strongly spin-orbit coupling[1]. The SOC produces an effect that is called band inversion that may give rise to two different phases: the before mentioned topological insulators or the Weyl-Dirac semimetals (Fig. 1.3). In this last phase, electrons mimic Weyl fermions and inherit many of their unique properties [13] (see Ch. 2.1.1).

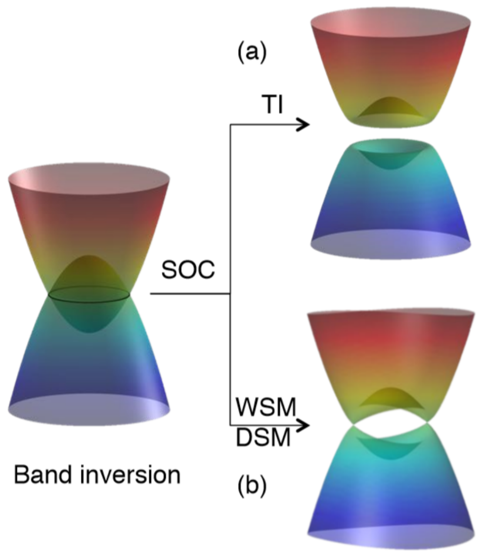

Figure 1.3: Topological insulator and Weyl or Dirac semimetal. The topology of both a TI and a WSM/DSM originates from similar inverted band structure. (a) The spin-orbit coupling opens a full gap after the band inversion, giving rise to metallic surface states on the surface of a TI. (b) In a WSM/DSM, the bulk bands are gapped by SOC in the momentum space except at some isolated linearly crossing points, called Weyl points/Dirac points, as a 3D analogue of graphene. Taken from [8].

[1]SOC describes a weak magnetic interaction of the electrons spin with their orbital motion; it is a relativistic effect which is responsible for many different aspects of the atomic structure.

In these materials the energy band, in specific momentum space regions, would obey Dirac or Weyl equation, with linear energy band dispersion [8]. What's more, this dispersion relationship can be topologically protected, which means that the linearity would be preserved as long as the system symmetry is not broken.

For sake of clarity, in Fig. 1.4 are sketched the signature features of band diagrams of different kinds of materials.

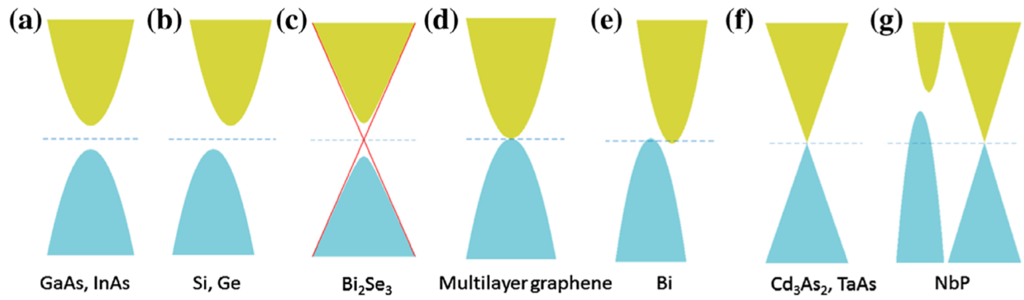

Figure 1.4: (a) Direct bandgap semiconductor. (b) Indirect bandgap semiconductor. (c) Topological insulator. (d) Semimetal with valance band and conduction band touching. (e) Semimetal with valance band and conduction band overlapping in different momentum point. (f) Topological semimetal with linear energy dispersion in the bulk. (g) Topological semimetal with additional hole pocket near the Weyl point. Taken from [14].

1.3 Properties of Weyl semimetals

The non-trivial topology of Weyl semimetals leads to many different transport mechanisms; all of them are in some way related to a characteristic effect which consists in an apparent violation of charge conservation, known as chiral anomaly. The most important mechanisms are the following [14]:

1. Shubnikov-de Haas oscillations;
2. Fermi arcs transport;
3. Non-local transport;
4. Thermoelectric transport.

The chiral anomaly is a peculiar effect of WSMs, that arises when a magnetic field is applied, thus generating Landau levels[2] in the energy bands. The dispersion relation can be expressed as [13]:

$$\epsilon_n = v_F \, sign(n)\sqrt{2\hbar|n|qB + (E \cdot B)^2}, \quad n = 0,\, 1,\, 2,\, ... \tag{1.2}$$

Where v_F is the Fermi velocity, $\hbar$ is the reduced Plank constant, q is the electron charge and E, B are the applied electric and magnetic fields.

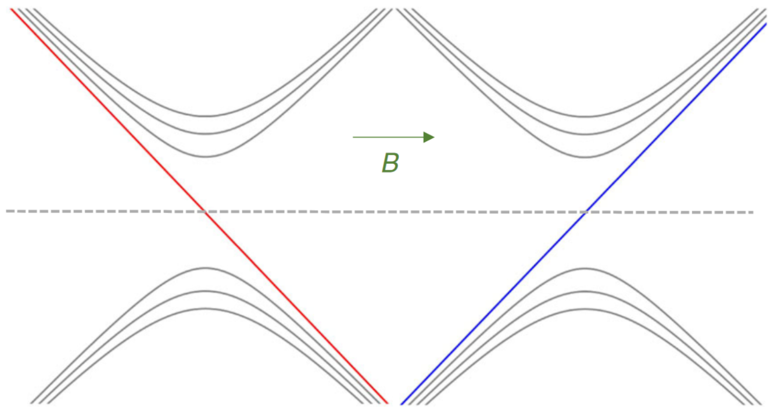

Figure 1.5: Landau levels splitting induced across a couple of Weyl points: the red and blue lines represent the 0^{th} LL of each node (linearly dispersing).

[2]LLs are the results of the quantization of the orbits of charged particles when subjected to a magnetic field.

Eq. 1.2 demonstrates that if an electric field is applied parallel to the magnetic field (i.e. the $E \cdot B$ term is not vanishing), a charge imbalance is induced between Weyl nodes, thus generating the chiral anomaly effect. The charge imbalance induced by the $E \cdot B$ term requires large momentum scattering process to relax [14]: a longitudinal current associated with chiral anomaly effect is generated, translating into a negative magnetoresistance. NMR should gradually disappear when the direction of the magnetic field deviates from the electric field direction, which is confirmed by the angle-dependent experiment reported in Fig. 1.6 (right panel).

The chiral anomaly-induced NMR was firstly observed in $Bi_{0.97}Sb_{0.03}$ crystal [15], which is identified as Dirac semimetal (the Weyl nodes are degenerate): when an external magnetic field is applied, the degeneracy is removed by splitting the single Dirac point into two separate Weyl nodes along the magnetic field direction and thus a Dirac semimetal is formally transformed into a Weyl semimetal.

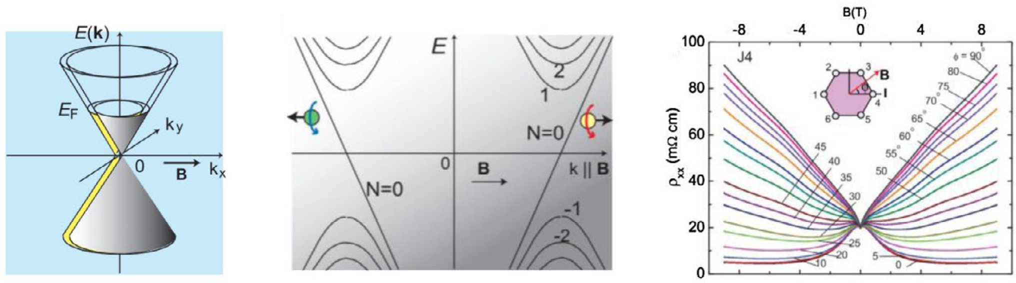

Figure 1.6: Left panel: the Dirac cone shift under external magnetic field. Central panel: the chiral anomaly effect. Right panel: the angle dependent experiment of magnetotransport. Taken from [15].

Shubnikov-de Haas oscillation is a transport mechanism which is usually the one that is detected in transport experiments to confirm the unusual phase in materials whose energy band satisfies linear energy dispersion, like those in Weyl semimetal near the Weyl nodes. SdH oscillation is again related to the Landau quantization of electronic states when subjected to high magnetic field. Under this condition, the magnetoresistance is reported to oscillate with a period depending on the inverse of the applied field [15]. The oscillations are due to the Fermi level which periodically crosses one and subsequent Landau level. Associated with the SdH oscillations, a huge magnetoresistance can be observed when the magnetic field is perpendicular to the driven current: these high values of MR (above 4 million % at 2 K [16]) are ascribed to a protection mechanism that significantly suppresses back-scattering at zero magnetic field, resulting in a high mobility and a transport lifetime times longer than the usual quantum lifetime. By removing this protection with the application of a magnetic field, the magnetoresistance naturally rises, with a quasi-parabolic behaviour (Fig. 1.7, left panel). However, the reason why this protection mechanism exists and why the shift of FS in momentum (i.e. the LL splitting due to the applied field) could lift the protection remains questionable; up to the present moment, the mechanism of large MR in topological semimetals still remains an open question [17].

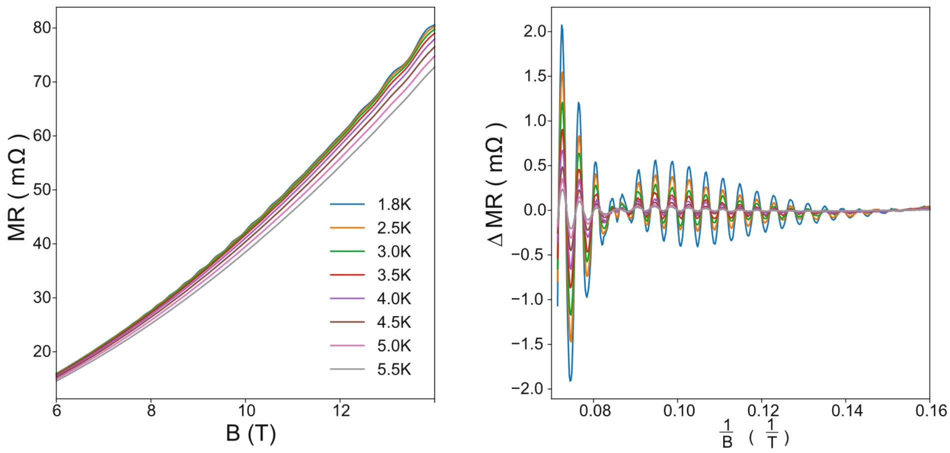

Figure 1.7: On the left: field dependence of the resistance of bulk $MoTe_2$ measured at ambient pressure. On the right: the corresponding SdH oscillations. Taken from [15].

The Fermi arcs transport is a particularly interesting mechanism since it is the only one of the before mentioned that is related to the topological nature of WSMs. The actual transport mechanism is called anomalous quantum oscillations and it is usually very difficult to isolate from bulk contribution [18]. When a magnetic field is applied perpendicular to the surface of a Weyl semimetal, it is able to produce a cyclotron orbit in which electrons slide along a Fermi-arc on the top surface, transfers to the bulk chiral LL mode of the node on which they propagate to the bottom surface, traverse the bottom Fermi-arc and return to the top surface via the mode with the opposite chirality [18]. This mechanism will be the starting point for the analysis of coherent field generation (Ch. 3); a detailed explanation of the Fermi arcs formation is reported in Ch. 2.2.

1.3.1 Type-I and Type-II Weyl semimetal

The first discovered family of WSMs (TaAs family [4]) exhibits ideal Weyl cones in the bulk band structure, with the FS that shrinks to a point at the Weyl node;

such kind of behaviour makes the TaAs family a type-I Weyl semimetal [8]. It can happen that the constant energy surfaces are open rather than closed and the resulting constant energy surfaces are electron and hole pockets. This second class of WSMs, which share the same topological and electronic behaviour of the first one, is called type-II WSMs. They are expected to support a variant of the chiral anomaly effect, that arises when the magnetic field direction is well aligned with the tilt direction, having a density of states different than the usual form, and possess novel quantum oscillations and anomalous Hall conductivity[3] [19]. The most relevant compounds belonging to this class are $MoTe_2$, WTe_2 and WP_2 [5].

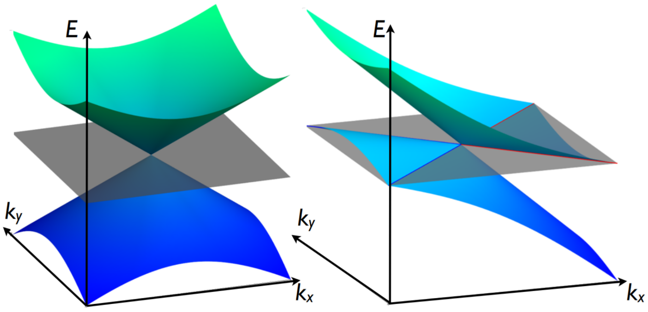

Figure 1.8: Type-I WSM with point-like Fermi surface at the Weyl node (left panel). Type-II WSM with electron and hole pockets (right panel). Taken from [19].

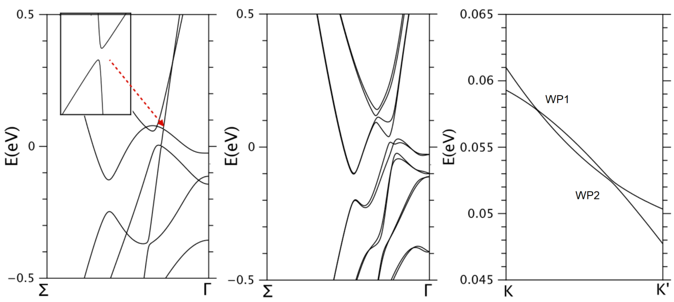

Figure 1.9: Band structure of WTe_2 (type-II), with and without SOC (left and center panels, respectively). Couple of Weyl points in the Brillouin zone (right panel). Taken from [19].

[3]The Hall effect is a phenomena that consists in the generation of a voltage difference across an electrical conductor due to the Lorentz force induced by an applied magnetic field. The Hall conductivity is therefore related to the transverse magnetoresistance.

1.4 Motivation and purposes

It is already clear that Weyl semimetals exhibit extremely interesting and unique transport and material properties. With this work, the intention is to show a path towards the utilization of these properties in electronic devices with impact in real-world applications. In particular, two main device concept will be deeply analysed:

1. First, an in-depth study on some particular aspects of the physics of Weyl fermions will be deepened, highlighting the possibility of exploiting a peculiar helical trajectory for the generation of a coherent oscillating field. This can represent the starting point for developing an RF oscillator, optimized to work at low temperatures and capable of delivering a very stable and controllable output field;

2. The second concept that will be presented is a device model of a Weyl semimetal cryogenic amplifier, which will be shown to exhibits significantly high gain with an improvement in the power consumption, thanks to its specific design and the enabling features of WSMs. The proposed design is intended to be a possible replacement for CMOS and HEMT technologies, which at the present moment are the only ones that are capable to work at very low temperatures [20][21].

Both the proposal are intended as possible solutions for state of the art quantum computers: the actual technology of qubits requires in fact both a good amplification (since the output signal is generally very low), and an RF signal to control and switch the qubit itself [20]. Moreover, quantum computers require extremely high performance in terms of bandwidth and noise, in order to ensure accuracy and speed in the control of the qubits and also to not disturb the quantum state of the qubit. The system integration of the proposed devices can allow for a significant reduction of the complex interconnections between the cryogenic chamber and the room-temperature electronics. This translates into an enhanced reliability, which is obviously needed in the creation of practical quantum computers [21]. The cryogenic devices are also needed in other areas, such as space applications or high-energy physics experiments, where extremely low noise is essential.

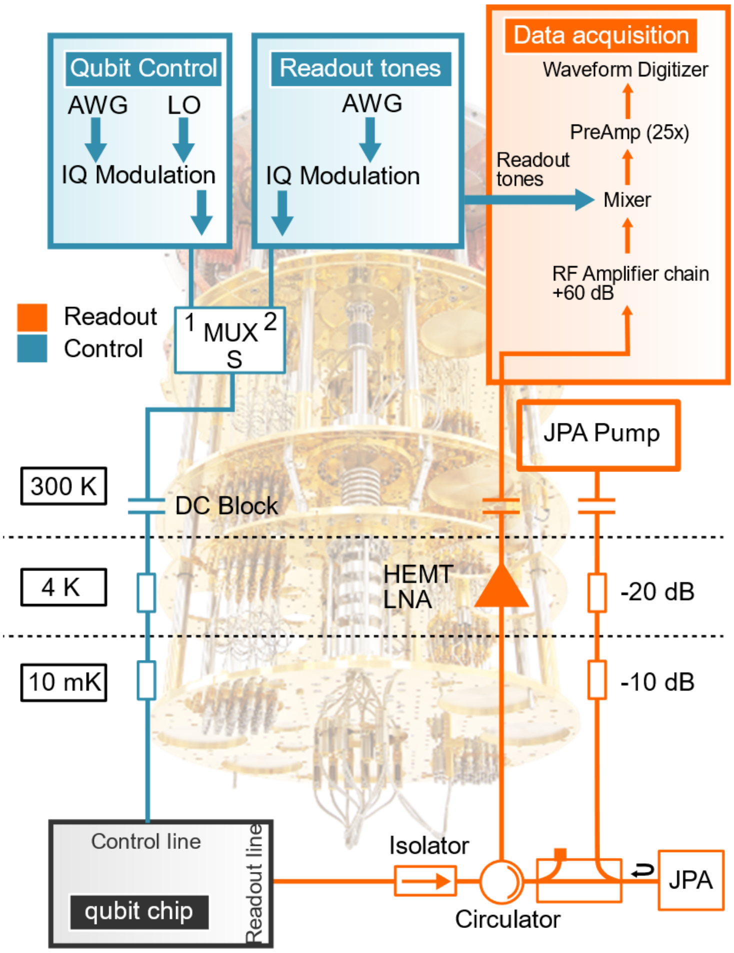

Figure 1.10: Building blocks of a qubit chip: notice the presence of both cryogenic amplifiers (in the readout block) and oscillating signal generators (control block). Courtesy of IBM.

Chapter 2

Physics of the Weyl semimetals

2.1 Weyl theory

Before actually getting to the description and characterization of the proposed devices, an overview of the relevant aspects of Weyl physics is presented, in order to get acquainted with the peculiarities of WSMs that allow for the developing of possible applications. The starting point of this description is obviously the Weyl equation.

The Weyl equation is a simpler form of the Dirac equation, which was first written in 1928 as a relativistic equation for a fermion field; however, when Dirac talked about fermion, he had primarily electrons in mind [22] (the title of the article in which he proposed his equation is in fact "The Quantum Theory of the Electron”). Electrons are particles with well-defined mass and charge, so when Weyl showed that for massless fermions, a simpler equation would suffice, it was clear that the Weyl fermions were not electrons. In 1930, Pauli proposed the neutrino to explain the continuous energy spectrum of electrons coming out in beta decay; the neutrinos had to be uncharged because of charge conservation, and they seemed to have vanishing mass from the analysis of beta decay data. It was therefore conjectured that the neutrinos are massless and consequently it made sense that they were Weyl fermions, whose properties could be described by Weyl theory. However, at the beginning of 1960s, the consequences of small but non-zero neutrino masses started to be considered, in order to detect them: if neutrinos have mass, they cannot be Weyl fermions; so what are Weyl fermions?

2.1.1 Weyl fermions

Weyl fermions are massless chiral fermions that embody the mathematical concept of a Weyl spinor and they can be realized as quasi particles in a low-energy condensed matter system [23]. The materials that exhibit this kind of excitation are called Weyl semimetals. In order to understand the physics that is required to describe the behaviour of the Weyl fermions, it is useful to start by the description of the Weyl equation itself. In its compact form, the Weyl equation has the expression reported in Eq. 1.1, where the σ matrices are the Pauli matrices (Eq. 2.1).

$$\sigma_1 = \begin{bmatrix} 0 & 1 \\ 1 & 0 \end{bmatrix}, \quad \sigma_2 = \begin{bmatrix} 0 & -i \\ i & 0 \end{bmatrix}, \quad \sigma_3 = \begin{bmatrix} 1 & 0 \\ 0 & -1 \end{bmatrix} \tag{2.1}$$

The plane-wave solutions of this equation are the so-called Weyl spinors:

$$\psi(\mathbf{r}, t) = \chi \, e^{\frac{\mathbf{p}\cdot\mathbf{r} - Et}{i\hbar}} \tag{2.2}$$

Where $\mathbf{p}$, $\mathbf{r}$ are respectively the momentum and position operators, t is the time and E is the eigenenergy. The term χ is a two component spinor, so the Weyl equation can be factorized in two coupled equations that take the form:

$$\begin{cases} (E - |p|)\psi_1 = 0 \\ (E + |p|)\psi_2 = 0 \end{cases} \tag{2.3}$$

It is possible to show how the solutions of Eq. 2.3 are the eigenstates of the helicity operator [24], which represents a crucial quantity for the understanding of the behaviour of Weyl fermions. In its general definition, the helicity of a particle is the projection of the spin onto the direction of momentum: a particle is said to be right-handed if the direction of its spin is the same as the direction of its motion and left-handed if it is the opposite.

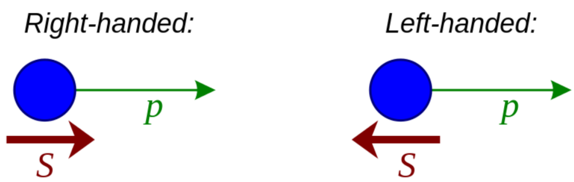

Figure 2.1: Graphical representation of the helicity of a moving particle.

So far, it was established that, in the massless limit, the fundamental fermion states are eigenstates of the helicity operator. For a massless particle with half-integer spin, the helicity operator is equivalent to the chiral operator[1]. By means of the chirality concept, we can obtain the Hamiltonian of the fermions by writing the Weyl equation as follows [3]:

$$i\hbar\frac{\partial}{\partial t}\psi = \chi\, p\psi \tag{2.4}$$

With $\chi = \pm 1$ being the chirality. Then, the Hamiltoninan can be expressed as [3]:

$$H(\mathbf{k}) = \chi\hbar v_F\,\mathbf{k} \tag{2.5}$$

From which we can observe the linear dispersion that in fact characterizes the band structure of WSMs. Also, given the 3D nature of the wavevector, there is no way to gap out the system: even adding a perturbation term $\tilde{H}(\mathbf{k})$ would only shift in the momentum space the position of the Weyl nodes. The geometric localization of the Weyl nodes can be visualized by explicitly separating the components of the Hamiltonian:

$$H(\mathbf{k}) = f_0(\mathbf{k})\mathbb{I} + f_1(\mathbf{k})\sigma_x + f_2(\mathbf{k})\sigma_y + f_3(\mathbf{k})\sigma_z \tag{2.6}$$

Where $\mathbb{I}$ is the identity matrix and the f functions are complex envelopes that carry the dependence of the Hamiltonian on the wavevector [3]. If we consider the situation where $f_1(\mathbf{k})$ vanishes in momentum space we would end up with a 2D surface that separates positive and negative values of the function. If we demand also $f_2(\mathbf{k})$ and $f_3(\mathbf{k})$ to be simultaneously zero, this specifies the intersection of three independent surfaces, which will occur at a point, namely a Weyl node. By adding a perturbation that changes the three functions by a small amount, this will also displace the zero surfaces and their intersections by a small amount, but the intersection will persist, just at a different crystal momentum [3]. This is the remarkable protection mechanism that distinguishes WSMs from 2D materials with analogue linear dispersion (such as graphene [25]).

[1] Massless particles appear to spin in the same direction along their axis of motion regardless of the point of view of the observer.

2.2 Fermi arcs

Now that we have understood the fundamental nature of Weyl fermions, we want to address a simple yet comprehensive explanation of the band structure of Weyl semimetals. WSMs are in fact characterized by a peculiar band structure that closes at isolated points in the Brillouin zone: these points are called Weyl nodes. At a spatial surface, the bulk band topology produces unusual surface states (Fermi arcs), whose Fermi surface consists of disjoint arc segments that connect surface projection of Weyl nodes with opposite chirality [13].

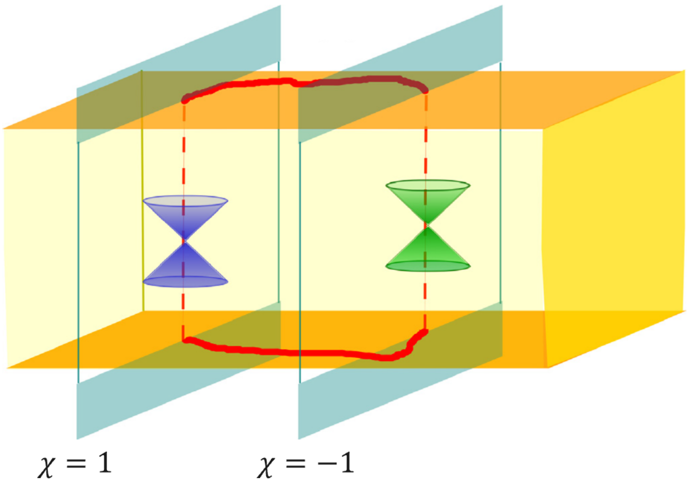

Figure 2.2: Weyl semimetal slab with a pair of Weyl nodes of opposite chirality; the surface has unusual Fermi arc states that connect the projections of the Weyl points on the surface. Taken from [13].

These surface states are said to be topologically protected since they do not vanish if the surface of the WSM is in contact with an other material or if the surface is peeled-off: this protection comes from the fact that WSMs are 3D material, as it can be seen by the corresponding Hamiltonian (Eq. 2.5). The Fermi arcs are different from the Fermi surface of a TI, an ordinary insulator or a normal metal, which are commonly a closed loop: therefore, the detection of Fermi arc surface states offer a strong evidence to identify a WSM. This is usually performed by means of a surface-sensitive characterization technique, such as angle-resolved photoemission spectroscopy or scanning tunnel microscope [26].

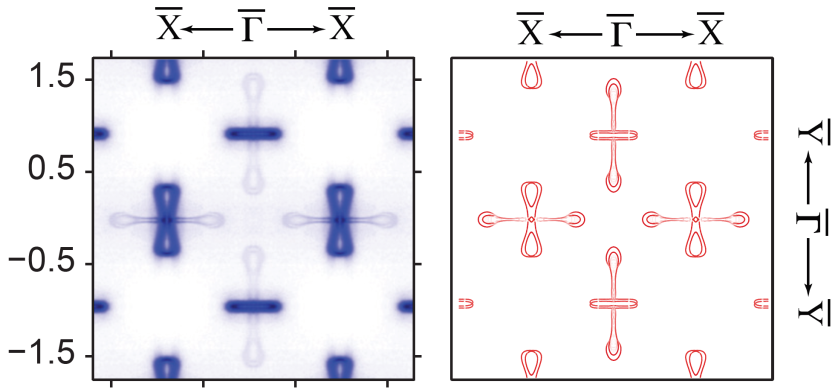

Figure 2.3: Fermi arcs of TaP from ARPES (left panel) and theoretical calculations (right panel): the two results agree very well. Taken from [8].

2.2.1 Weyl nodes

In order to clearly understand why this particular surface states arise, we need to better define the concept of Weyl nodes (or Weyl points). In solid-state band structures, Weyl fermions exist as low-energy excitations of the Weyl semimetal, in which bands disperse linearly in three-dimensional momentum space through a node which is called Weyl point. The quantity that is used to characterize the topological entanglement between conduction and valence bands is called Berry curvature, which is equivalent to a magnetic field in the momentum space. The Berry curvature becomes singular at the Weyl points, that act as monopoles in the momentum space with a fixed chirality. Therefore, a Weyl point can be a source ($\chi = +1$) or a sink ($\chi = -1$) of the Berry curvature (see Fig. 2.2).

The relationship between chirality and Berry curvature can be expressed as follows [13]:

$$\chi = \frac{1}{2\pi} \oint_{FS} \mathbf{F}(\mathbf{k}) \mathrm{d}\mathbf{S}(\mathbf{k}) \tag{2.7}$$

Where $\mathbf{F}(\mathbf{k})$ is the Berry curvature (or Chern flux). Since the total magnetic charge in a band structure should be zero [27], it is immediate to verify that there must be as many nodes with positive chirality as the negative ones, that is why the Weyl points always appear in pairs. Moreover, the fact that the Weyl nodes are chiral and are monopoles of magnetic flux is what generates the previously introduced chiral anomaly. In simple words, the number of quasi-particles around Weyl nodes of fixed chirality is not conserved in the presence of parallel electric and magnetic fields, which are able to pump charge between Weyl nodes of opposite chiralities (Fig. 2.4).

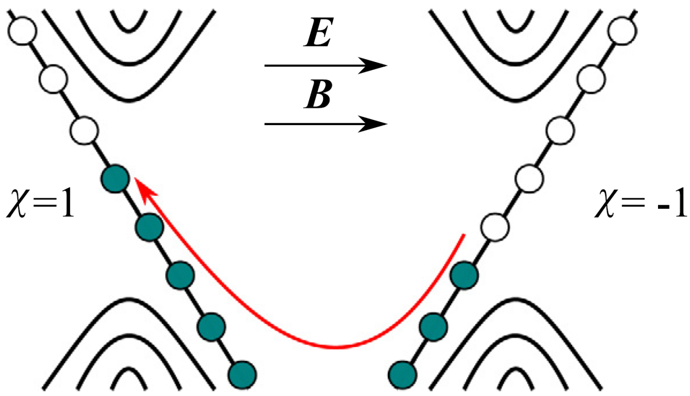

Figure 2.4: Charge pumping between Weyl nodes in parallel electric and magnetic fields; each point in the dispersion is a Landau level (taken from [13]).

Now that we have understood the physical origin of Fermi arcs and how they are related to the position of the Weyl nodes in the momentum space, we can proceed with a detailed description of the anomalous quantum oscillations, which are the signature effect of the topological nature of Fermi arcs.

The analysis of this mechanism and how it can be exploited for actual applications will be delivered in Ch. 3.

Chapter 3

Coherent field generation by Weyl fermions

3.1 Cyclotron orbits in Weyl semimetals

The possibility of achieving a coherent generation of an oscillating field from a WSM relies on the unusual closed magnetic orbits that are observed in these materials [28]. Despite Fermi arcs being disjoint, when an external magnetic field is applied, the electrons are able to travel from surface to surface thanks to the presence of the so-called Landau levels [18]. This mechanism is the foundation of the work presented in this chapter, which aim to exploit the unique thickness-dependence of the orbit time to produce a controlled, coherent electromagnetic field.

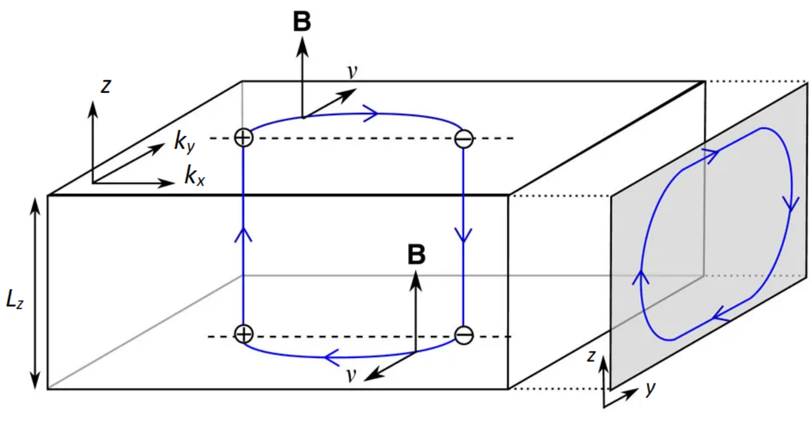

Figure 3.1: Cyclotron orbit of the electron in the hybrid space. Adapted from [18].

The description of the behaviour of electrons inside a WSM when subjected to a magnetic field will be carried out as follows:

1. First, a semi-classical picture of the 2D trajectory of a single electron will be presented, highlighting the signature dependence of the orbit time on the slab thickness;
2. Then, it will be reported an overview of a simple quantum model that provides a comprehensive description of the actual magnetic orbits of the electrons;
3. Lastly, an elliptical approximation of the 2D trajectory is introduced, in order to obtain a semi-classical equation of motion, which will be expanded with the addition of the drifting component, due to the application of an electric field perpendicular to the magnetic one.

The field generated by the resulting 3D trajectory will be further analysed, starting from a single-electron model and then moving to a more complete framework in which the effect of more than one electron in the conductive slab is considered. In particular, it will be presented a coherency condition which is required in order to have the electrons moving in phase, thus producing constructive interference and keeping the signature thickness-dependence of the frequency of the generated field. A detailed description of the relationship between the quantities involved will be presented, focusing on the degree of freedom that we have when designing a proper experimental setup for the generation of the oscillating output field.

3.1.1 Semi-classical model

As previously stated, it is well established that applying a uniform magnetic field along a direction perpendicular to the longitudinal axe[1] of a WSM slab forces the electrons to move along a cyclotronic orbit [18]. In the semi-classical framework, this motion is described with an orbit time defined as reported in Eq. 3.1.

$$t_{orbit}(B) = \frac{2L_z + 2k_0 \cdot l_B(B)^2}{v_F} \tag{3.1}$$

In Eq. 3.1, L_z is the slab thickness and k_0 is the rest length of the Fermi arcs. The magnitude of the magnetic field affects the orbit time through the quantity l_B (magnetic length), which is defined in Eq. 3.2.

$$l_B = \sqrt{\frac{\hbar}{qB}} \tag{3.2}$$

[1]The axes frame of reference will follow the notation of Fig. 3.1, unless otherwise specified.

Eq. 3.1 assumes that the electrons are travelling at fixed velocity (the Fermi velocity, v_F), along closed rectangular loops, whose dimensions are respectively the thickness of the WSM slab and the real space projection of the Fermi arcs. It is worth noticing how the topological protection of the surface states (the Fermi arcs) forces the electrons to travel always from surface to surface, no matter what is the magnetic field applied. This is a key feature that distinguishes the WSMs from classic metals and allows for the possibility of achieving a coherent field generation [29].

However, the semi-classical approximation does not completely hold since the actual trajectory is not an ideal rectangle (it is pierced at the corners). A more complete way to model the trajectory is through a proper quantum description of the cyclotron motion: Ch. 3.1.2 and 3.1.3 will be dedicated to this topic.

3.1.2 Quantum model: two-band Hamiltonian

The semi-classical model used in the introduction of this chapter works well as a preliminary description of the ideal behaviour of the trajectory of the electrons in the 2D cross-section and gives an immediate idea of the frequency of the output field through the orbit-time. In order to have a more detailed description of the cyclotron orbit, we will exploit a quantum mechanical model for the oscillations. The starting point of this analysis consists in the description of the Landau splitting of the energy bands when subjected to an external magnetic field (as previously stated, the LLs are the "conveyor belt" that joins together the top and bottom Fermi arcs). The model used for the quantum description of the trajectory exploits a two band Hamiltonian that can be written as follows [30]:

$$H = A(k_x\sigma_x + k_y\sigma_y) + M_k\sigma_z \tag{3.3}$$

Where the σ matrices are the Pauli matrices, k_x, k_y and k_z are the three component of the electrons wave-vector, A is the vector potential and M_k is defined as: $M_k = M(k_0^2 - k_{el}^2)$, with M being a model parameter.

The dispersion of the two energy bands can be simply written as:

$$E = \pm\sqrt{M_k^2 + A^2(k_x^2 + k_y^2)} \tag{3.4}$$

In Fig. 3.2 it is shown the model band structure: it describes a couple of Weyl nodes located at (0,0,$\pm k_0$).

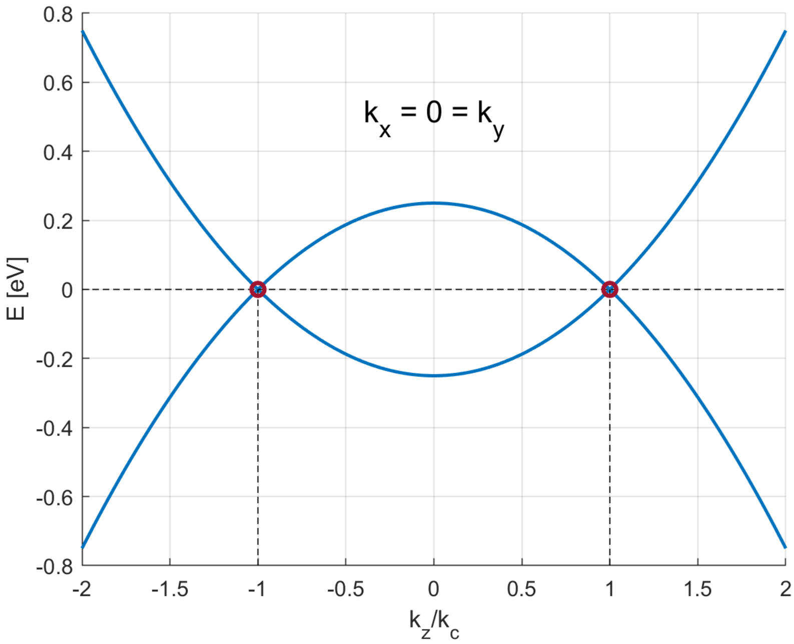

Figure 3.2: Energy dispersion of the model Hamiltonian of a WSM slab along the (0, 0, k_z) orientation.

The set of parameters used to obtain Fig. 3.2 are:

$$\begin{cases} A = 0.25 \text{ eV} \\ k_0 = 1 \text{ nm}^{-1} \\ {L_y}^2 = 40 \text{ nm} \\ M = 0.25 \text{ eV/nm}^2 \end{cases}$$

The next step is devoted to highlight the presence of the characteristics of Fermi arc surface states (at $k_x = 0 = k_y$ they collapse in the Weyl nodes). Since the WSM slab with has a finite thickness L_y, the wave-vector component k_y should be viewed as an operator in the Hamiltonian. The electronic eigen-solution of the WSM slab is reported in Fig. 3.3.

[2]In this chapter the frame of reference is different with respect to the one reported in Fig. 3.1. The slab has an infinite width L_x (to avoid dealing with boundary conditions) and a finite thickness L_y. This choice is made since the orbital motion is purely 2D, so we do not need a third component.

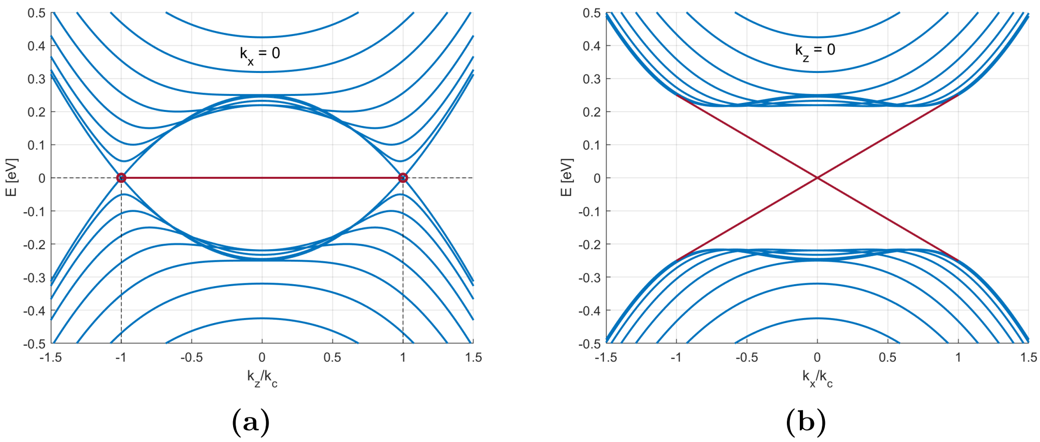

Figure 3.3: Energy dispersion of the model Hamiltonian of a WSM slab as a function of k_z (3.3a) and k_x (3.3b), for $k_y \in [0{,}2k_0]$; the red lines represents surface Fermi arcs.

We can notice how, by sweeping the y component of the electrons wave-vector, the presence of the Fermi arcs is highlighted. Within the present two-band model, the surface states have linear dispersion with respect to k_x, but independent of k_z (Eq. 3.5).

$$E_{Arc} = \pm A\, k_x \tag{3.5}$$

The plus/minus sign means that the surface states are chiral in the sense that they support only one-way, opposite propagating modes.

This structure of the WSM slab is obviously modified in the presence of a vertical magnetic field, which is the enabling feature for the the cyclotron motion of the electronic wave packet, through the LLs. The electronic band structure of bulk WSMs described by Eq. 3.3 can be analytically solved, but the process is not trivial; here for simplicity we only report the obtained results (Fig. 3.4, see [31] for the mathematical steps involved).

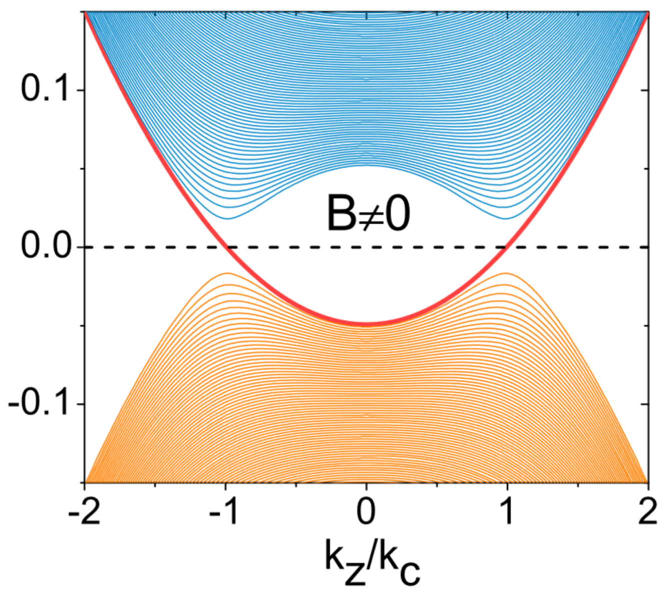

Figure 3.4: Landau levels of the WSM slab in a perpendicular magnetic field ($B_y = 0.1$ T) at $k_x = 0 = k_y$; the 0^{th} Landau levels are highlighted in red. Taken from [31].

3.1.3 Quantum trajectory

Once it is established how the energy dispersion of the WSM slab modifies when subjected to a perpendicular magnetic field, it is possible to evaluate the quantum trajectory of an electronic wave-packet. The whole derivation is reported in [30]; in the following only the key steps will be highlighted, together with the final results.

The time-zero wave-function is defined as:

$$\Psi(k_x, y, z, t = 0) = g(k_x)\psi(0) \tag{3.6}$$

Where $g(k_x)$ is a Gaussian component that is not affected by the applied field and $\psi(0)$ is the product of another Gaussian propagator (along the z direction this time) with the topological surface state of the WSM in absence of magnetic field. The electronic wave-function at an arbitrary later time t can be obtained by adding an exponential time propagator, and it has the following expression:

$$\Psi(k_x, y, z, t) = e^{-i\frac{Ht}{\hbar}}\Psi(k_x, y, z, t = 0) \tag{3.7}$$

The position expectation values of the x and y components of the motion is then expressed as:

$$\begin{cases} x(t) = \langle \Psi | \hat{x} | \Psi \rangle \\ y(t) = \langle \Psi | \hat{y} | \Psi \rangle \end{cases} \tag{3.8}$$

Whose behaviour is shown in Fig. 3.5.

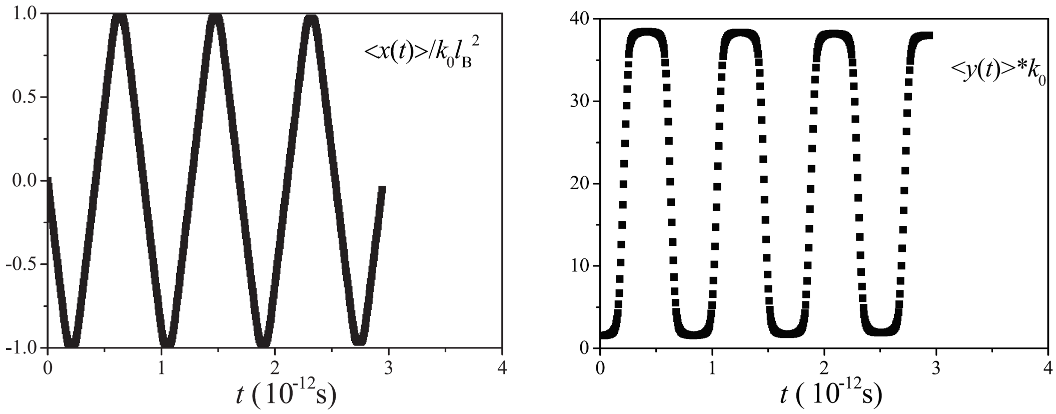

(a) **(b)**

Figure 3.5: Electronic coordinate expectation value as a function of time. Adapted from [30].

Fig. 3.5a shows how the electronic wave-packet oscillates periodically between $\pm k_0 l_B^2$, which in the momentum space means a periodic motion between the two Weyl nodes along the Fermi arc. By looking at Fig. 3.5b it is possible to see how in the y direction the electronic wave-packet transmits through the bulk to the opposite surface whenever it arrives at a Weyl node. By combining the two results together, we can obtain a graphical representation of the actual 2D trajectory of an electron inside a WSM slab.

The resulting behaviour is shown in Fig. 3.6.

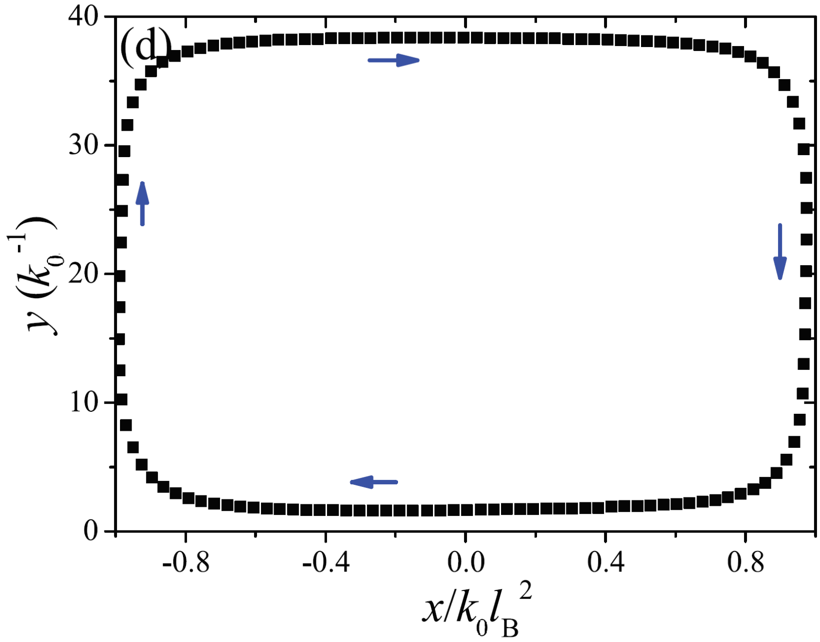

Figure 3.6: Cyclotron orbit of the initial electronic wave packet as given by Eq. 3.6 in a vertical magnetic field. Blue arrows indicate the motion direction of the electronic wave packet along the cyclotron orbit. Adapted from [30].

Notice that the y coordinate is expressed in nanometers, while the x coordinate is normalized to the length of the Fermi arcs in the real space. We can see that the actual trajectory is not different from the purely rectangular motion described by the semi-classical model.

3.1.4 Elliptical approximation

The 2D quantum trajectory gives us an exact representation of the motion of an electronic wave-packet in a WSM when subjected to a magnetic field. However, this solution is difficult to handle and to exploit for further calculations. To overcome this problem, we propose an approximation that is able to merge together the information provided by both the semi-classical and the quantum models. The trajectory in fact can be well approximated by an ellipse in the (y, z)[3] plane.

[3]We switch back to the frame of reference of Fig. 3.1.

The equation of motion of the y and z components is reported in Eq. 3.9.

$$\begin{cases} y(t) = a(B) \cdot cos\Big(\omega(t - t_0) - \theta_0\Big) - y_0 \\ z(t) = b \cdot sin\Big(\omega(t - t_0) - \theta_0\Big) \end{cases} \tag{3.9}$$

Where ω is the orbit frequency, $a(B)$ and b are respectively the major and minor semi-axes of the ellipse and t_0, θ_0 and y_0 are parameters introduced to model the noise effects (a complete description of the noise model is reported in Ch. 3.3.2).

The resulting trajectory is reported in Fig. 3.7.

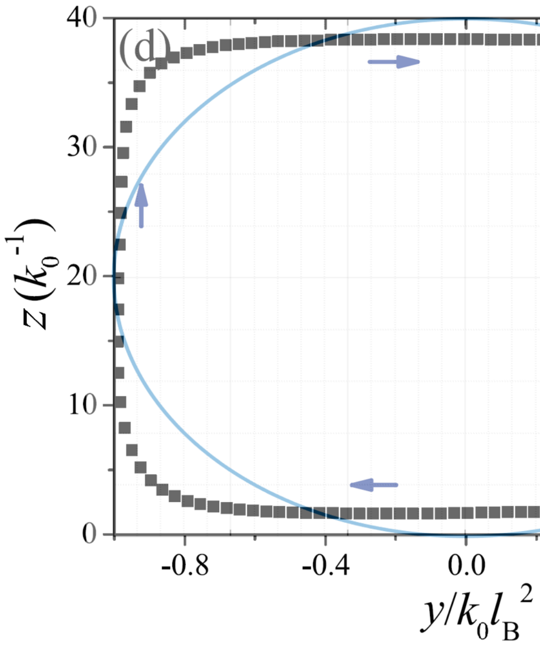

Figure 3.7: Superposition of the elliptical approximation of the trajectory with the one obtained with the quantum model.

The elliptical approximation agrees quite well with the quantum trajectory and offers an analytical formulation of the equation of motion. This will enable the possibility to achieve a rather simple, close-form expression of the coherency condition, as reported in Ch. 3.3.

3.2 3D trajectory: the drift effect

The main problem of 2D quantum oscillations is that they are difficult to detect. In particular, depending on the doping level, the geometry of the slab and the value of the applied field, there can be a destructive effect coming from bulk oscillations, that makes the surface ones very hard to measure [18]. In order to overcome this problem, the effect of an electric field applied perpendicular to the magnetic one is considered.

It is reasonable to predict that, if we inject electrons in the WSM slab by applying an electric field perpendicular to the (y,z) plane (the axis orientation follows the notation used in Fig. 3.1), the electrons will move on an helical path, thus tunneling from a couple of Weyl nodes to the next ones (the levels are discrete), while keeping their orbital motion. In this way we are forcing a population imbalance that drives an electron flow that, given its exotic trajectory, will produce an oscillating field in the time domain. The classical experimental techniques aimed at the detection of quantum oscillations usually report the oscillating behaviour of the resistivity (or some other detectable quantity that depends on the density of states) with respect to the inverse of the applied magnetic field. The working principle is the following: the variation of the external magnetic field causes the Landau levels to periodically cross the Fermi surface, which results in oscillations of the density of states at the Fermi level (Fig. 3.8).

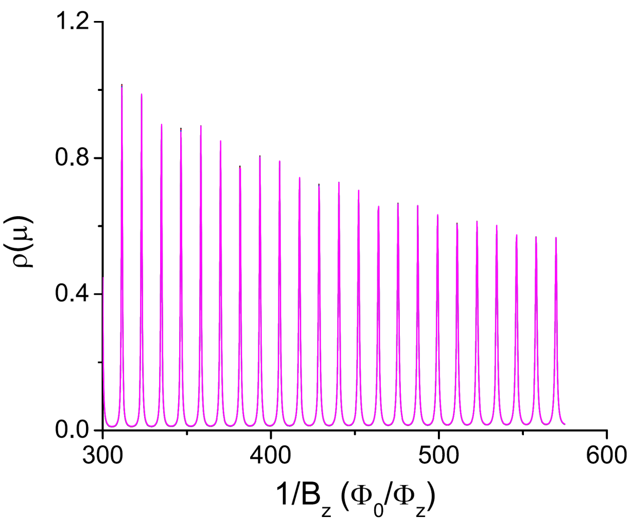

Figure 3.8: Density of states as a function of the inverse magnetic field (normalized), for a Weyl semimetal slab of thickness $L_z = 63\ nm$. Taken from [18].

3.2.1 Single-electron field

In Fig. 3.9 is reported a schematic of the motion of one electron in a WSM when subjected to crossed magnetic and electric filed. The 2D trajectory is evaluated according to the elliptical approximation described by Eq. 3.9. The drifting component of the motion (the one ascribed to the electric field) is described by the following expression:

$$x(t) = -\frac{L_X}{2} + \mu \sum_{i=1}^{n} \mathrm{rect}(t - i\, t_d - \frac{1}{2}) E_{drift}(B) \cdot (t - i\, t_d) \tag{3.10}$$

Where L_x is the length of the WSM slab, μ is the electron mobility, t_d is the drift time, E_{drift} is the applied drift field and n is the average number of electrons in the channel. The complete expression of the equation of motion is reported in Eq. 3.11; the point $\mathrm{P}(X_P, Y_P, Z_P)$ is the sensing point.

$$\mathbf{r}(t) = \sqrt{[X_P - x(t)]^2 + [Y_P - y(t)]^2 + [Z_P - z(t)]^2} \cdot \hat{u}_r \tag{3.11}$$

The resulting trajectory is depicted in Fig. 3.9.

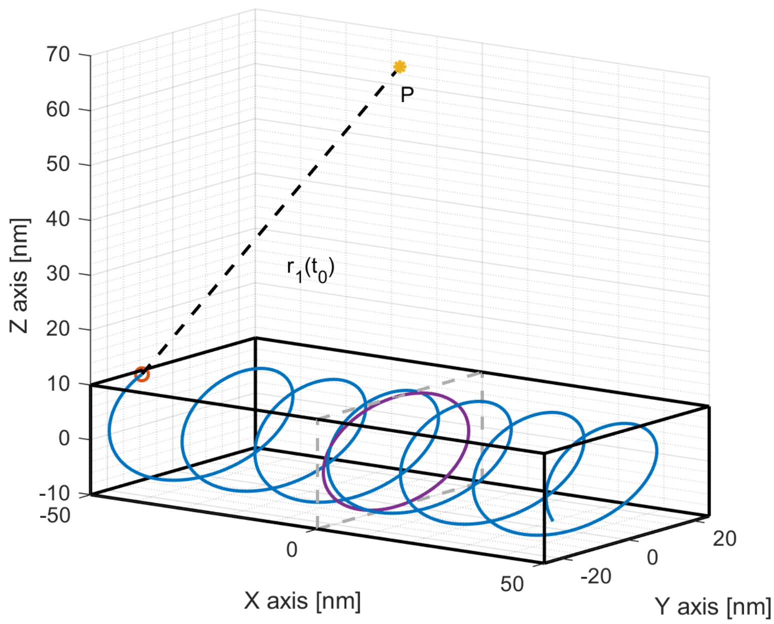

Figure 3.9: Schematics of the motion of a single electron inside the WSM.

For the evaluation of the field produced by a particle that moves in this way, it is possible to use the simple non-relativistic expression, since the electrons move at the Fermi velocity, which is orders of magnitude lower than the light velocity [18] (Eq. 3.12).

$$E(\mathbf{r}) = \frac{q}{4\pi\epsilon_0}\mathbf{r}^{-2} \tag{3.12}$$

Where ϵ_0 is the electric permittivity of vacuum and $r(t)$ is the previously reported equation of motion.

The field generated in P by a single particle moving according to Eq. 3.11 is reported in Fig. 3.10.

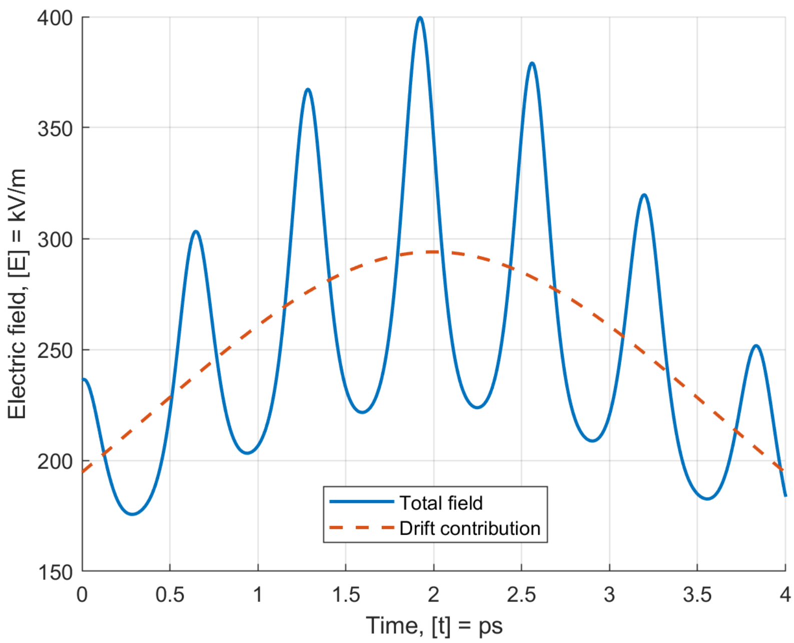

Figure 3.10: Superposition of the field generated by a linear drift and the the total output field generated by a single electron moving across the WSM.

In Fig. 3.10, it is also highlighted the drift contribution to the total field. i.e the field that would be produced by an electron moving across the slab along a linear path, without oscillations. We can notice that the exotic trajectory of the electrons is able, according to the performed simulation, to generate an electric field which oscillates with period equal to the orbit time.

3.3 Coherency conditions

Up till now, it was only considered the case where there is one electron flowing inside the channel, which is not what happens in real materials where we usually have more than one electron per time flowing inside the WSM slab. The question that we need to address now is what happens to the output field when we have n electrons inside the channel.

In order to accomplish this task, we enforce the following assumptions:

1. First, as already discussed, the motion of the electrons in the cross-section is supposed to be perfectly elliptical;

2. The injection of electrons is restricted only to a superficial contact area, with perfectly ohmic contacts;

3. The injection position of the electrons may vary randomly, thus introducing a phase delay (noise).

The average number of electrons flowing inside the WSM slab depends on different parameters like the dimensions of the slab, the material properties and also the applied drift field which is responsible for the current inside the WSM. In the following section, it will be described how it is possible to select a value of the applied field that is able to produce a coherent output field, at steady-state condition (i.e. for every electron that is collected at the end of the slab, one electron is injected).

3.3.1 Steady-state behaviour

By looking again at Fig. 3.9 it is possible to predict that the condition that is able to produce a coherent output is the one where we have the electrons inside the channel equally spaced (approximately one electron per ring), oscillating in phase. This condition, that seems very strict at the beginning, can be achieved quite easily just by selecting a proper value for the applied electric field. This is made possible by the fact that, since the contacts are perfectly ohmic, and the channel itself is made by a semimetal that, by definition, does not offer a potential barrier to overcome, the electrons are strongly correlated, i.e. they tend to minimize the reciprocal repulsion by arranging themselves in an equally spaced condition. Given the finite length of the slab, the current that must be set in order to have an average number of electrons in the channel that matches the ratio between drift time and orbit time is the following:

$$I = \frac{q}{t_{orbit(B)}} \tag{3.13}$$

Which means that the applied electric field can be expressed as:

$$E_{drift}(B,T) = \frac{\frac{qv_F}{2L_z+2k_0\cdot l_B^2(B)}}{L_yL_z\frac{\sigma_0}{1+\mathrm{MR}(B,T)}} \tag{3.14}$$

Where $\mathrm{MR}(B,T)$ is the magnetoresistance, whose modeling represents a key aspect for the Weyl semimetal amplifier (Ch. 4) and σ_0 is the zero-field conductivity.

Now it is possible to substitute in Eq. 3.12 both the expressions of $\mathbf{r}(t)$ and E_{drift} (Eq. 3.11 and 3.14), thus obtaining the complete expression that was used to evaluate the coherent field generated by the current flowing inside the WSM slab (Eq. 3.15).

$$E_P(t) = \frac{q}{4\pi\epsilon_0}\left\{\left[X_P + \frac{L_x}{2} - \mu\sum_{i=1}^{n} rect(t - it_d - \frac{1}{2})E_{drift}(B)\cdot(t - it_d)\right]^2 + \left[Y_P - a(B)\cdot cos(\omega(t-t_0)-\theta_0) - y_0\right]^2 + \left[Z_P - b\cdot sin(\omega(t-t_0)-\theta_0)\right]^2\right\}^{-2} \tag{3.15}$$

The behaviour of the generated output field is shown in Fig. 3.11.

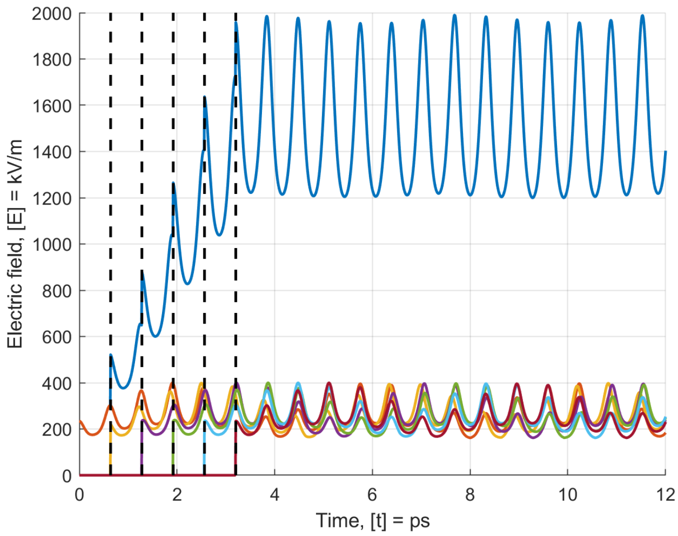

Figure 3.11: Total electric field in $\mathrm{P}(X_P, Y_P, Z_P)$.

Notice how at each dashed line an electron is injected, until the steady-state regime is reached. The small de-phasing between the single electron fields is due to thermal noise.

3.3.2 Quantum noise

As previously stated, the strong correlation between the electron translate into a shot noise suppression: the only relevant contribution to noise is the thermal noise[4], whose power spectral density can be evaluated as reported in Eq. 3.16.

$$P_{th} = \frac{4k_B T}{R} \tag{3.16}$$

In Eq. 3.16, k_B is the Boltzmann constant, T is the average temperature and R is the WSM resistance. It follows that the noise contribution to the drift current is given by:

$$I_{th} = \sqrt{4K_B T \frac{\sigma_0}{1 + MR(B,T)} \frac{L_y L_z}{L_x}} \tag{3.17}$$

Since thermal noise is a statistic effect, in order to properly analyze its impact on the coherency of the output, a Monte Carlo analysis of the behaviour of the device was performed. The obtained results are reported in Fig. 3.12.

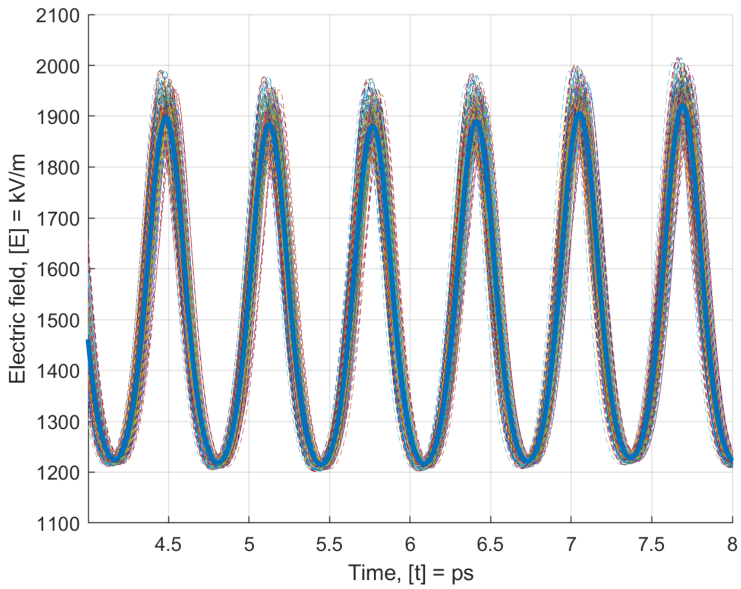

Figure 3.12: Monte Carlo analysis of the steady-state field produced at $T = 2\ K$, $B = 1.5\ T$. The blue line represents the average field.

[4]The validation of this sentence and the derivation of Eq. 3.16 and 3.17 are delivered in Appendix B.

It is clear that, at this conditions, the thermal noise has an almost negligible impact on the performance of the device. However, the previously shown simulations were performed at cryogenic temperature (which are the standard working conditions for this kind of detection [32]), so it may be reasonable to predict that at room temperature even thermal noise can cause a severe de-phasing of the single electron contributions.

In Fig. 3.13 is reported the behaviour of the simulated device at room temperature. It is possible to see how there are almost no changes with respect to Fig. 3.12. This is due to the fact that the magnitude of the thermal current is rather small (fractions of pA), but also because the current density inside the WSM is considerably high.

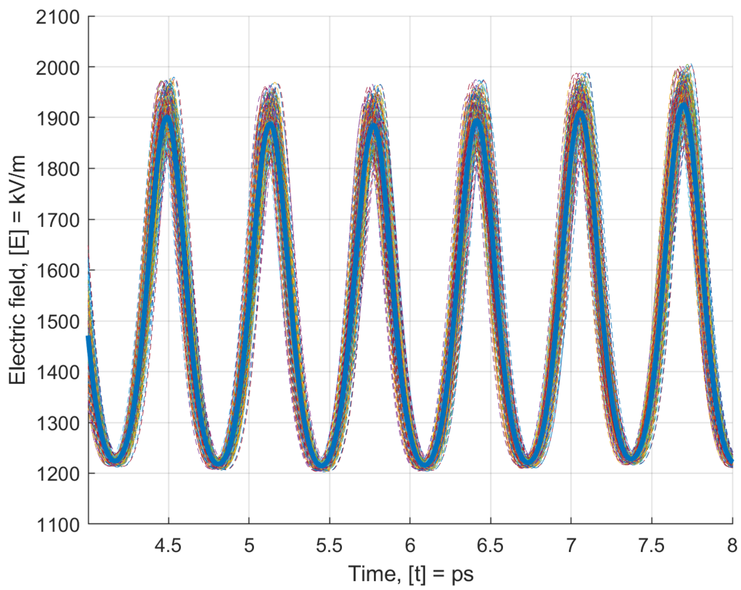

Figure 3.13: Monte Carlo analysis of the field produced at $T = 300\ K$, $B = 1.5\ T$.

If we perform the same simulation at lower magnetic field the situation is considerably different. In this case, at room temperature the magnitude of the noise becomes comparable to the magnitude of the current itself, resulting in a damping of the amplitude of the output field (Fig. 3.14).

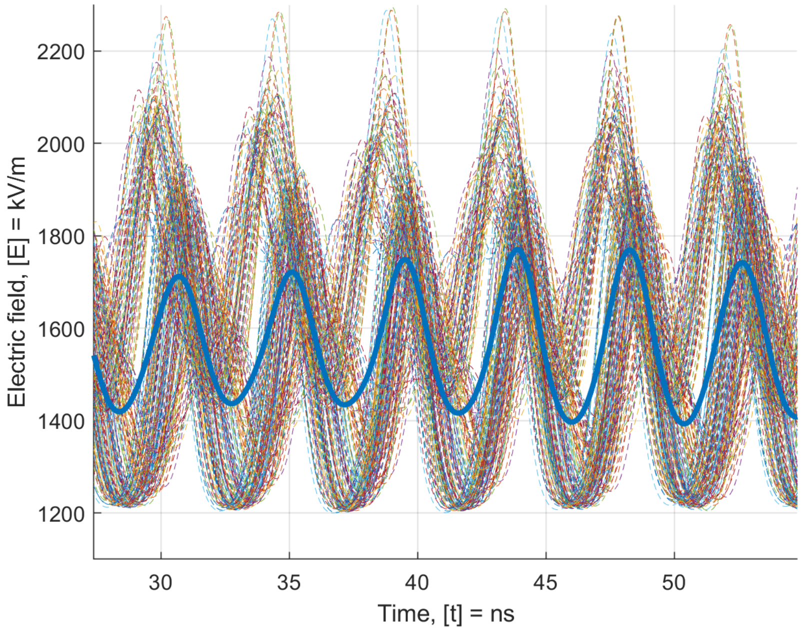

Figure 3.14: Monte Carlo analysis of the field produced at $T = 300\ K$, $B = 150\ \mu T$.

It will be shown in Ch. 3.4.1 that in order to observe quantum oscillations, rather high values of magnetic field are required. This translates into a trade-off between the geometry of the slab, the applied magnetic field, the frequency of the output field and the noise level.

The noise problem can be always solved by going down to cryogenic temperatures. Moreover, in Fig. 3.14, despite a considerable noise level, the average frequency of the oscillation is preserved, thus proving the robustness of the generation mechanisms enabled by the unique properties of WSMs.

3.4 Device concept: Weyl semimetal oscillator

These results indicate that topological transport in Weyl semimetal could generate coherent oscillations, which has not been reported before. According to the calculations performed here, these oscillations could even be visible at room temperature. A promising application for this effect is in a voltage-controlled oscillator: since the VCO action is generated by a single device, it could operate at significantly lower power dissipation than a CMOS counterpart. However, further work is needed to elucidate the potential of such a device, in particular there are some practical issues that need to be overcome before proposing an actual device implementation.

3.4.1 Perspectives and limitations

One of the most stringent requirement for the oscillations to take place concerns the applied magnetic field: having established the existence of quantized magnetic orbits involving Fermi arcs does not imply that these orbits produce quantum oscillation. For this to happen, the magnetic field should satisfy to the following equation [33]:

$$B_n = \frac{\hbar k_0}{q\left[\frac{\hbar \pi v_F}{\mu}(n+1) + L_z\right]}, \qquad n : B_n > 0 \tag{3.18}$$

Where μ is the chemical potential. Moreover, the applied field should be below the saturation value, which is approximately equal to [18]:

$$B_{sat} \approx \frac{\hbar k_0}{q L_z} \tag{3.19}$$

For field values above this threshold, the majority of the magnetic orbit takes place in the bulk, thus losing the thickness dependence which is the key to coherence. However, the value of the saturation field is rather high (a few dozen Tesla, depending on the thickness and the rest-length of the Fermi arc), and so this is generally never the case [18]. It has to be noticed that, even at lower fields, a bulk contribution is always present and it can potentially interfere with a coherent output generation. A possible way to filter out the bulk contribution is playing with the doping level: in fact when the chemical potential lies in the chiral region (Fig. 3.15) only surface states contribute to quantum oscillation.

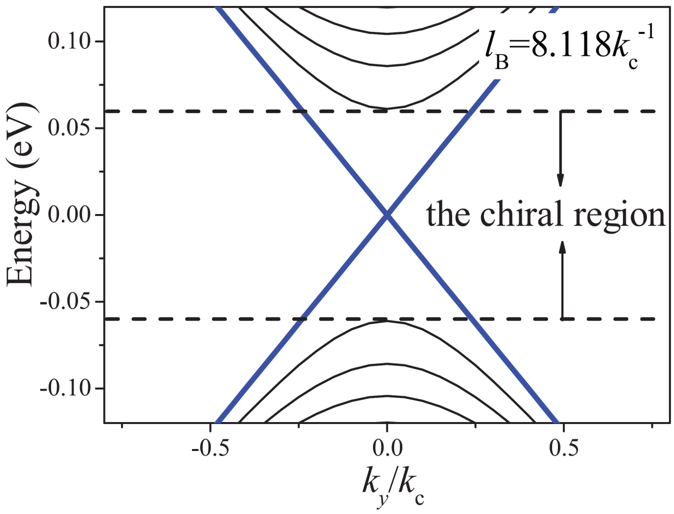

Figure 3.15: Energy spectrum of a bulk WSM immersed in a perpendicular magnetic field. Blue lines represent bulk chiral Landau bands, which are the ones required for having a coherent output field. The reported value of the magnetic length corresponds to approximately 8.5 T (assuming $k_0 = 0.1\ nm$). Taken from [30].

A second issue related to the magnetic field is the possible presence of a low-threshold below which the quantum oscillations are not able to take place.

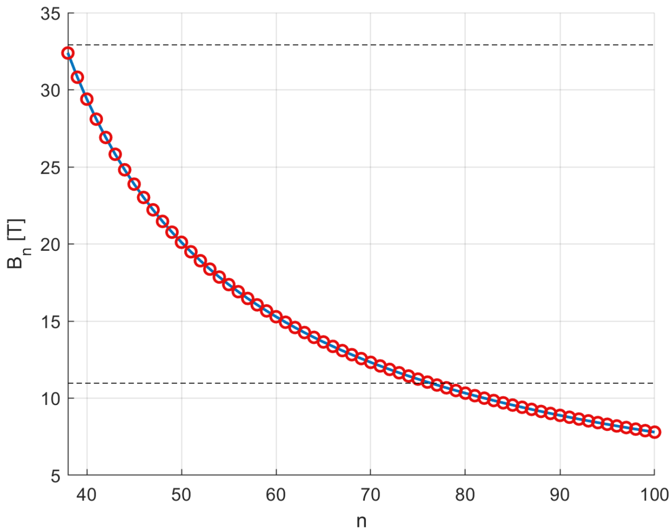

Figure 3.16: Graphical interpretation of Eq. 3.18. The dashed lines represent the upper and lower threshold fields.

We know in fact that the spacing between the Weyl nodes depends on the magnetic field through the magnetic length. When dealing with a finite-width slab, there are values of the magnetic field for which the trajectory of electrons is apparently out of the cross-section.

Let's for example consider the simple two-bands model that led to Fig. 3.6: assuming a Fermi arc length of 0.1 nm and an applied field of 10 T, we would obtain a trajectory width of approximately 120 nm. Depending on the actual width of the slab[5], this requirement identifies a minimum value of the field that has to be applied in order to allow for quantum oscillations to take place. This pose a concrete trade-off in a possible device implementation, since the output frequency depends on the magnetic field. The free parameters that we have in the design of a Weyl semimetal oscillator are essentially two: k_0 and L_y. In particular, the rest-length of the Fermi arcs is a strongly material-dependent quantity which can vary of several orders of magnitudes, leaving a discrete freedom in the tuning of the lower threshold.

In conclusion, in order to enlarge the operating window of the WSO, further analysis of materials properties is needed. At the moment, this work aims to represent a simple way to test the presence of Weyl semimetal phases in new materials, with Fermi arcs of different lengths, thus opening the path for a concrete device implementation.

[5]The lower threshold of Fig. 3.16 is evaluated at fixed width, according to: $B_{min} \approx \frac{\hbar k_0}{q L_y}$

Chapter 4

Weyl semimetal amplifier

4.1 Device model

The route towards quantum computing requires novel electronic devices that are able to perform efficiently at very low temperatures, with high reliability and significant noise reduction [20]. A possible solution for the implementation of such kind of devices is represented by Weyl semimetals. In this chapter, the device concept of a Weyl semimetal cryogenic amplifier is presented. It will be shown that the proposed device is in simulations able to perform significantly better the the actual competing technologies, being able to provide high power gain with a notable reduction of the required DC power.

The schematic of the proposed device is reported in Fig. 4.1. It consists of a simple gating of a Weyl semimetal channel, with an inter-layer of insulating oxide. The materials chosen are respectively: Niobium for the gate metal (which can exhibit superconductive behaviour, see Ch. 4.1.1), SiO_2 for the oxide interlayer and WP_2 for the WSM channel. The working principle of the device is a magnetoresistive coupling between the gate and the channel: when a bias is applied between the source and drain contacts, the gate metal produces a magnetic field all around it, thus tuning the magnetoresistence of the channel, which results in a modulation of the current flowing inside it. A graphical representation of the working principle of the device is shown in Fig. 4.2.

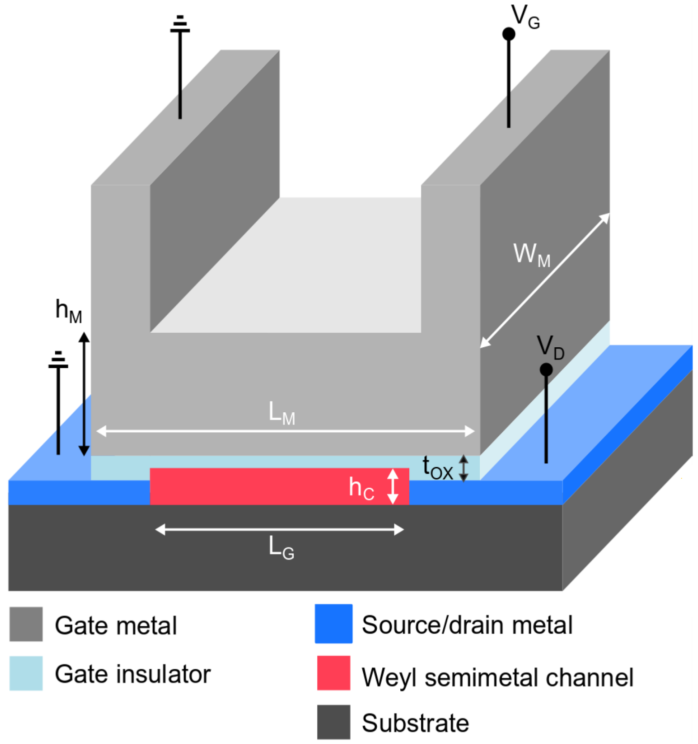

Figure 4.1: Schematic representation of the proposed WSM amplifier.

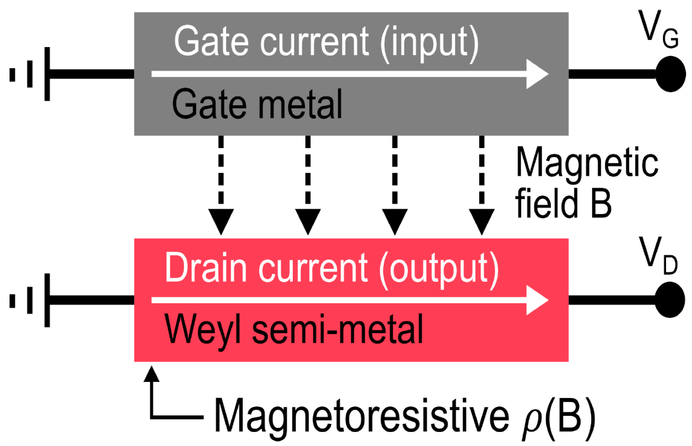

Figure 4.2: Schematic representation of the MR coupling between gate and channel.

Theoretically, the magnetoresistance is defined as the ratio between the zero-field resistivity and the resistivity shift under a magnetic field [16]:

$$MR = \frac{\rho(B,T) - \rho(0,T)}{\rho(0,T)} \tag{4.1}$$

Notice that, given the wire-shape of the WSM channel, the effective magnetic field that tunes the MR of the device is mainly directed perpendicularly to the direction of the current flow in the channel. The transverse magnetoresistance in WSMs usually exhibits a quasi-parabolic dependence on the applied magnetic field that is well fitted by Eq. 4.2 [16].

$$\rho(B,T) = \rho_0(T)\,[1 + (\alpha\, B)^m] \tag{4.2}$$

The parameters α and m are determined empirically: in most cases it holds that $m \in [1{,}5; 1{,}8]$; α instead has a wider range of values and it also depends on the temperature. It is worth noticing that in all the relevant literature [16][34], the α parameter is always taken outside the power m; in this work it was chosen to bring α inside the parenthesis in order to assign to it a precise physical meaning. In fact, written in this way, α has the dimension of an electronic mobility, which is the quantity that normalizes the density of flux (for a more detailed analysis on the MR modeling see Ch. 4.4.1).

4.1.1 Superconductive effect of the gate

As mentioned before, the gate of the device is made of Niobium, which is a type-II superconductor[1]: this choice is made in order to have ideally zero resistance inside the gate (low losses) and to generally optimize the performance of the device. In order to properly model the superconducting behaviour of the gate we need to solve Eq. (4.3), which is the London equation for the density of current [35].

$$\nabla^2 \mathbf{J} = \frac{1}{\lambda_L^2}\mathbf{J}^{\,2} \tag{4.3}$$

An analytical solution of this equation can be obtained in the 1D case, where the behaviour of $J(x)$ is an exponential decay (Eq. 4.4).

$$J(x) = J_0\, e^{-x/\lambda_L} \tag{4.4}$$

In Eq. 4.4, J_0 is the superficial density of current. The quantity λ_L is called London penetration depth and it is a material-dependent quantity that is used to

[1] A type-II superconductor exhibits an intermediate phase of mixed ordinary and superconducting properties at intermediate temperature and fields above the superconducting phases.

describe the so-called skin confinement effect of the supercurrent. The explanation of this effect can be addressed as follows: let's look again at Eq. 4.4 and consider that in $x = 0$ there is an interface between a non-superconducting material and a superconducting one; in this case, in the SC region, the current would be confined in a thin layer close to the interface between the two materials, according to Eq. 4.4.

A numerical solution of the 3D London equation can be obtained with a FEM solver: in Fig. 4.3 it is possible to observe the confinement effect previously described.

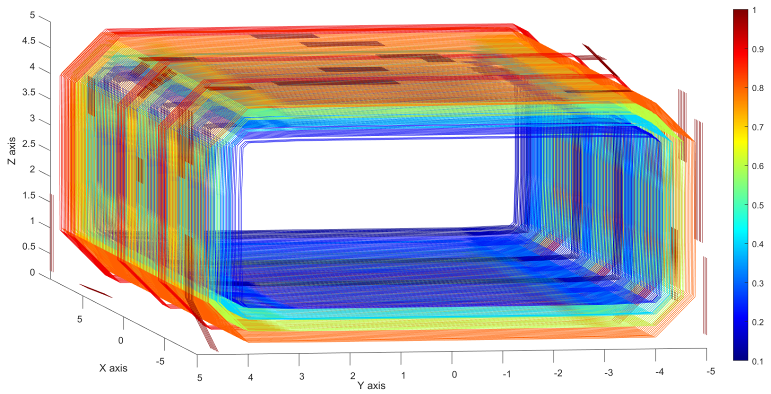

Figure 4.3: Sliced view along the X-axis of the current density profile inside the superconducting gate.

Notice that in Fig. 4.3 the dimensions of the slab are normalized and the London penetration depth is set significantly lower than its actual value (which for Nb is approximately equal to 39 nm [36]) in order to highlight the confinement effect. If the dimensions of the device are comparable to λ_L, then the SC density is not negligible inside the slab.

4.1.2 Effective field evaluation

Considering the space distribution of the super-current is a necessary step for the evaluation of the effective magnetic field that is produced by the current flowing inside the gate. The field evaluation is made according to the generalized Biot-Savart law, which is reported in Eq. 4.5.

$$\mathbf{B}(\mathbf{r}) = \frac{\mu_0}{4\pi} \int_V \frac{\mathbf{J}(\mathbf{r'}) \times (\mathbf{r} - \mathbf{r'})}{|\mathbf{r} - \mathbf{r'}|^3} d\mathbf{r'} \tag{4.5}$$

The quantity $\mathbf{J}(\mathbf{r'})$ is the density of supercurrent that comes out of the London equation.

If the dimension of the device are comparable to the London penetration depth, the previous equation can be simplified as follows:

$$\mathbf{B}(\mathbf{r}) = \frac{\mu_0}{4\pi} J_0 \int_V \frac{\mathbf{r} - \mathbf{r'}}{|\mathbf{r} - \mathbf{r'}|^3} d\mathbf{r'} \tag{4.6}$$

The actual computation of the field is made by discretizing the space inside the WSM channel (the one described by the coordinate $\mathbf{r}$) and then proceeding in the integral summation of all the contributes coming from the gate region (described by $\mathbf{r'}$).

In Fig. 4.4 is reported a graphical interpretation of the integral evaluation.

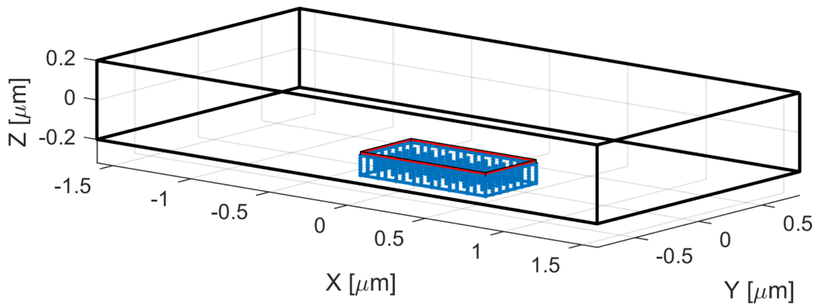

Figure 4.4: 3D schematic of the active region of the device with the grid points inside the WSM channel.

Notice that in Fig. 4.4 the dimensions of the WSM are merely indicative: the analysis of the optimization process that guided the design of the device is reported in Ch. 4.3.1.

The field distribution generated by a squared wire is reported in Fig. 4.5 (longitudinal cross-section).

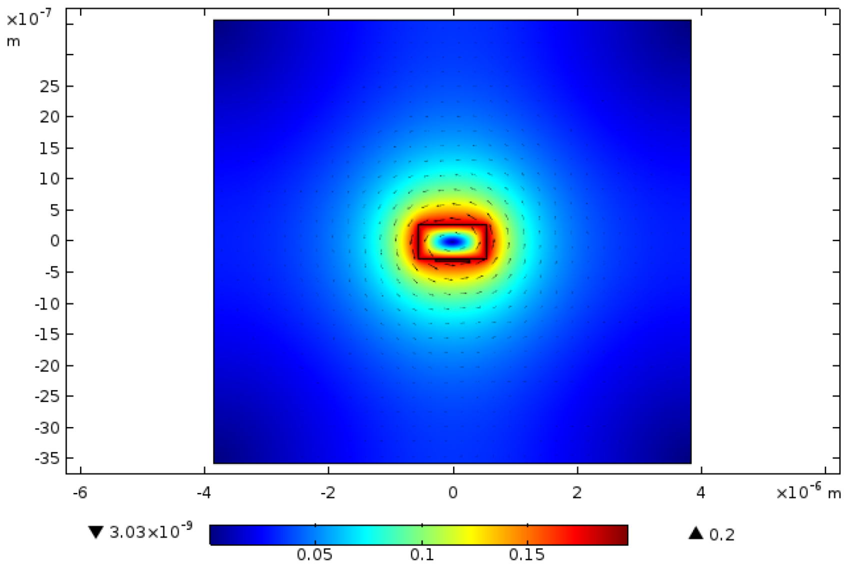

Figure 4.5: Sliced view of the magnetic flux density generated by a squared wire. Taken from [37].

We can see how the field is concentrated in the superficial region near the borders of the cross-section and its direction is mostly parallel to the sides. These results, together with the values obtained by the direct evaluation of Eq. 4.6, validates the use of Eq. 4.2 as fitting model for the MR, since most of the field is in fact perpendicular to the current flow.

4.2 Circuit model

The frequency characterization of the Weyl semimetal amplifier was performed by using a transfer function defined in terms of the so-called Y parameters. The basic circuit model for the device is reported in Fig. 4.6.

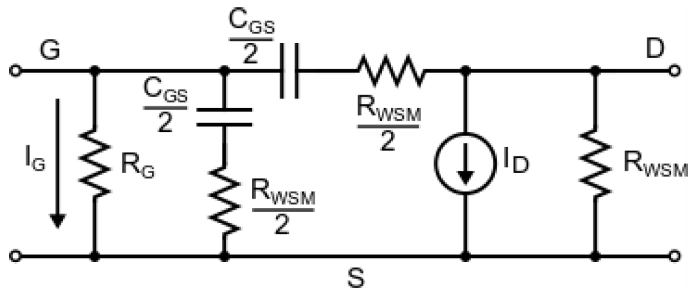

Figure 4.6: Small-signal model of the WSA.

This circuit model is quite standard and it is obtained directly from the physical model of the proposed device (Fig. 4.1) just by looking at each node and considering the electrical elements that connect them together. Since the device is a two-port device, the Y matrix is consequently 2x2; the corresponding Y parameters are defined as follows:

$$\begin{cases} Y_{11} = \frac{1}{R_G} + 2\frac{i\omega C}{1+i\omega RC} \\ \\ Y_{12} = -\frac{i\omega C}{1+i\omega RC} \\ \\ Y_{21} = g_m - \frac{i\omega C}{1+i\omega RC} \\ \\ Y_{22} = \frac{1}{R_{WSM}} + 2\frac{i\omega C}{1+i\omega RC} \end{cases} \tag{4.7}$$

Starting from this model, it is possible to express the power gain (which in the end is the most useful quantity to evaluate the performance of the proposed device) as:

$$P_G = \frac{|Y_{21} - Y_{12}|^2}{4|Re(Y_{11})Re(Y_{22} - Re(Y_{12})Re(Y_{21})|} \tag{4.8}$$

The obtained results and the impact of each quantity involved in this calculation is further analysed in Ch. 4.3.

4.2.1 Inductive effect of the gate

In order to model the behaviour of the device, one main improvement to the circuit model reported in Fig. 4.6 has been applied: the gate resistance in fact is not completely passive since the flux variation generates a non-zero inductance in the gate area. The value of R_G in the model has been replaced by a complex impedance defined as follows:

$$Z_G = R_G + i\omega L \tag{4.9}$$

Where L is the kinetic inductance[2] and is defined as:

$$L = \left(\frac{m_e}{2n_s q^2}\right)\frac{l}{A} \tag{4.10}$$

The frequency response of the device is reported in Fig. 4.7.

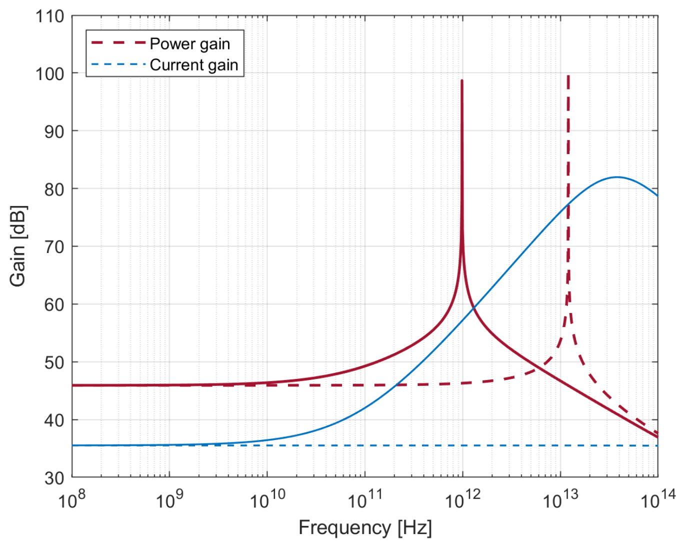

Figure 4.7: High-frequency characterization of the WSA; the dashed lines represent the results obtained with zero inductance.

It is possible to see that the non-zero inductance, which in the end is a parasitic effect, shifts the resonance peak at lower frequencies. Also the width of the peak is increased, since the Q factor, which is a standard quantity used to characterize resonators, is inversely proportional to the value of L.

[2]Kinetic inductance is a manifestation of the inertial mass of charge carriers that arises in conductors with very high carrier mobility at very high frequencies.

4.3 Device optimization

In order to understand and properly simulate the behaviour of the WSA, one of the most important quantity to analyze is the transconductance, which relates the current flowing through the output of a device to the voltage across its input. In formula it can be expressed as:

$$g_m = \left.\frac{\partial I_D}{\partial V_G}\right|_{V_{DS}} \tag{4.11}$$

The output conductance is easier to evaluate since it can be seen by the small-signal model that it is just the reciprocal of the channel resistance (the resistance of the WSM). Through these two quantity, it is possible to evaluate the current and voltage gain as follows:

$$\begin{cases} A_V = \frac{\partial V_{DS}}{\partial V_{GS}} = g_m \cdot R_{WSM} \\ \\ A_I = \frac{\partial I_{DS}}{\partial I_G} = g_m \cdot R_G \end{cases} \tag{4.12}$$

The power gain is then:

$$P_G = R_G \, R_{WSM} \, g_m^2 \tag{4.13}$$

The expression of the transconductance can be further expanded in order to analyze the impact that each quantity has on the device performance: this is a crucial step in the design of the device since both the geometry and the voltages play a relevant role in determining the performances of the amplifier. To do so, an explicit derivation of how the drain current depends on the gate voltage is needed.

Let's start from the basic definition of the drain current:

$$I_D = \frac{V_{DS}}{R_{WSM}} \tag{4.14}$$

Since the WSM resistance can be simply related to its resistivity, we can plug in Eq. 4.2 in the previous one, thus obtaining:

$$I_D = V_{DS} \frac{A_{WSM}}{l_{WSM}} \frac{1}{\rho_0[1 + (\alpha\langle B\rangle)^m]} \tag{4.15}$$

The last step consists into substituting Eq. 4.5 in Eq. 4.15: to lighten the notation as much as possible the Biot-Savart integral has been labeled as I_{BS}.

The final expression for the drain current is reported in Eq. 4.16.

$$I_D = V_{DS} \frac{A_{WSM}}{l_{WSM}} \frac{1}{\rho_0 \left[1 + \left(\alpha \mu_{red} I_{BS} \frac{V_G}{R_G A_G} \right) \right]} \tag{4.16}$$

By computing the derivative of the current with respect to the gate voltage, it is possible to obtain a detailed expression for the transconductance, which is reported in Eq. 4.17.

$$g_m = -V_{DS} \frac{A_{WSM}}{l_{WSM}} \frac{1}{\rho_0} \left(\alpha \mu_{red} \frac{I_{BS}}{R_G A_G} \right)^m \frac{m\, V_G^{m-1}}{\left[\left(\alpha \mu_{red} \frac{I_{BS}}{R_G A_G} \right)^m + V_G^m + 1 \right]^2} \tag{4.17}$$

By means of Eq. 4.17, we can predict the impact that each quantity has on the performance of the WSA. The easiest quantity to analyze is obviously V_{DS} since it can be immediately seen how the dependence is linear. The gate voltage instead has a trickier relationship with g_m: a graphical representation of the relationship is reported in Fig. 4.8.

The device dimensions used for the initial calculation were chosen on common sense principles and represent the basis of the optimization process that will be described. These values are reported in Tab. 4.1.

	Gate	WSM channel	Oxide layer
Length	500 nm	250 nm	250 nm
Width	250 nm	50 nm	50 nm
Height	50 nm	25 nm	25 nm

Table 4.1: Starting values for the design of the device.

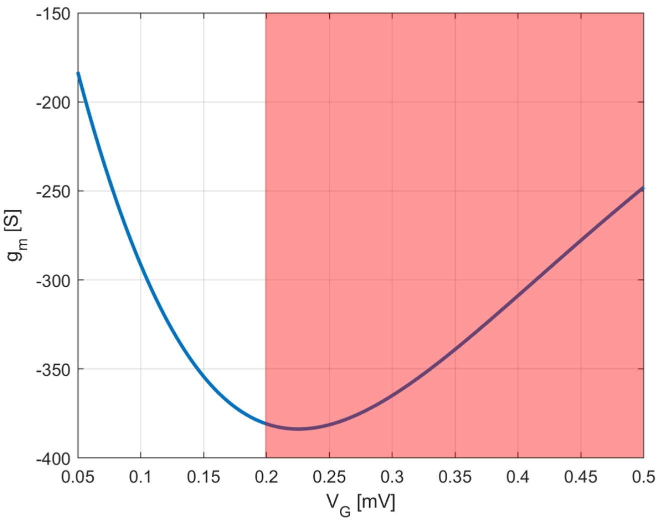

Figure 4.8: Graphical behaviour of the transconductance versus the gate voltage: the red region represent the values of the gate voltage that, given the geometry reported in Tab. 4.1, produces a current overshoot (the gate is not superconductive anymore).

Fig. 4.8 is incomplete since the gate voltage not only affects the transconductance but also the resistance of the channel. In order to fully analyze the impact of V_G on the power gain we need the complete expression of P_G, which is reported in Eq. 4.18 (the expression of g_m is kept implicit in order to avoid an heavy notation, its behaviour with V_G has been already discussed anyway).

$$P_G = \frac{R_G\, l_{WSM}}{\rho_0\, A_{WSM}} \left[1 + \left(\alpha \mu_{red}\, I_{BS} \frac{V_G}{R_G A_G}\right)^m\right] g_m^2 \tag{4.18}$$

In order to obtain a more understandable expression, it is possible to label all the terms that do not depend on V_G as c and the multiplicative factor as k: the obtained expression is reported below.

$$P_G \propto \frac{V_G^{2(m-1)}}{\left(1 + c + V_G^m\right)^4} \left[1 + (kV_G)^m\right] \tag{4.19}$$

In Fig. 4.9 is reported the behaviour of the power gain when changing V_G: it is possible to see that the device cannot operate at the maximum gain level since the gate voltage would be too high and the gate would loose its superconductive behaviour. In particular, the maximum allowed value of V_G for this geometry is around 0.2 mV.

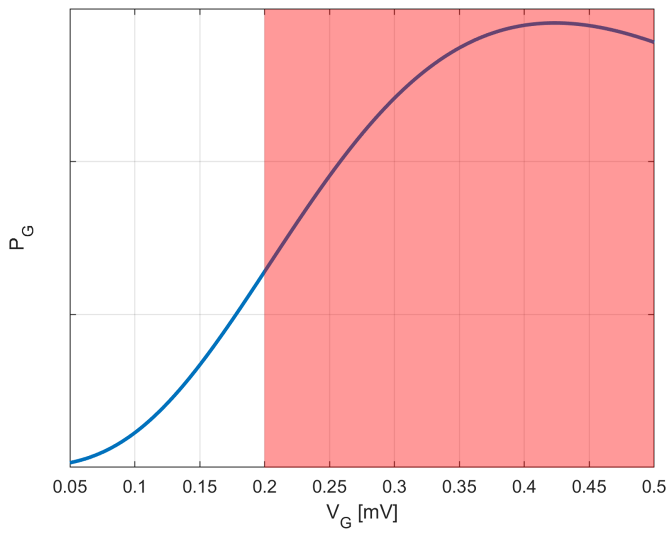

Figure 4.9: Power gain versus gate voltage (the magnitude of the power gain is not reported since in the calculation the multiplicative factors were omitted).

The last quantity that is interesting to discuss is the factor α: it is particularly relevant since it is the quantity that allows for the proper functioning of the device. In fact, if α is equal to zero, i.e. the MR is zero, there is no amplification at all. This sentence is obviously confirmed by the simulations: in Fig. 4.10 is reported the behaviour of the transconductance with α.

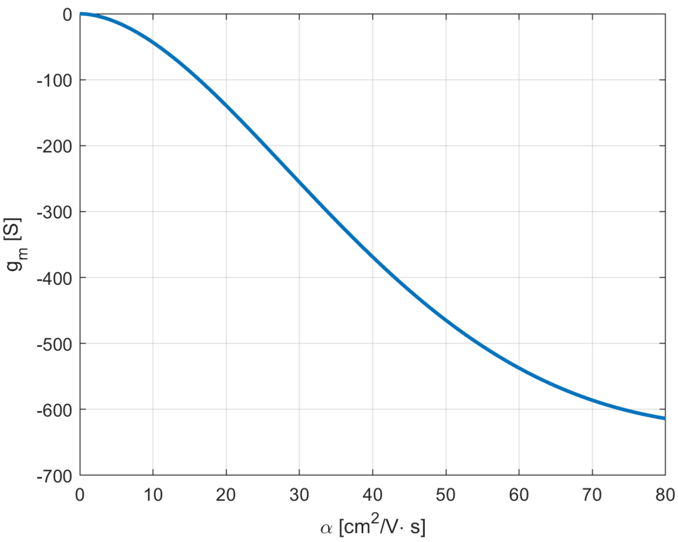

Figure 4.10: Transconductance versus α.

4.3.1 Scalability of the device and gain optimization

Before going into the detailed discussion of the obtained results for the frequency behaviour of the WSA, an overview of the criteria that guided the design of the device is presented: in particular the focus is on the reasons behind the choice of the device dimensions.

The first, and obvious, statement is that in principle you want to have a device which is as small as possible, in order to improve the integration density. This goal however usually comes at a cost: scaling down a device in fact has a deep impact on its performance and sometimes there are hard scaling limits that cannot be overcome without compromising the functioning of the considered device. With WSA the main scaling issue is related to the magneto-resistive modeling: at the moment there is not a clear understanding of the physical reasons behind MR and so it is not possible to establish how scaling down a magnetoresistive device might affect its behaviour (see Ch. 4.4.1 for further description).

Concerning the geometry of the device, there are several criteria that must be satisfied in order to maximize the performances of the WSA; in the following are reported and described the main criteria that guided this work.

The explicit dependence of Eq. 4.17 and 4.18 on each dimension is difficult to obtain since there are several quantities that are implicitly dependent on geometric parameters (all the resistances for instance) and moreover in both equations there is the integral contribution given by the Biot-Savart law that is difficult to read. For these reasons, a different approach was adopted: in Fig. 4.11 and 4.12 are reported a set of repeated analysis with only one dimension per time varying in a range of values around the starting ones reported in Tab. 4.1.

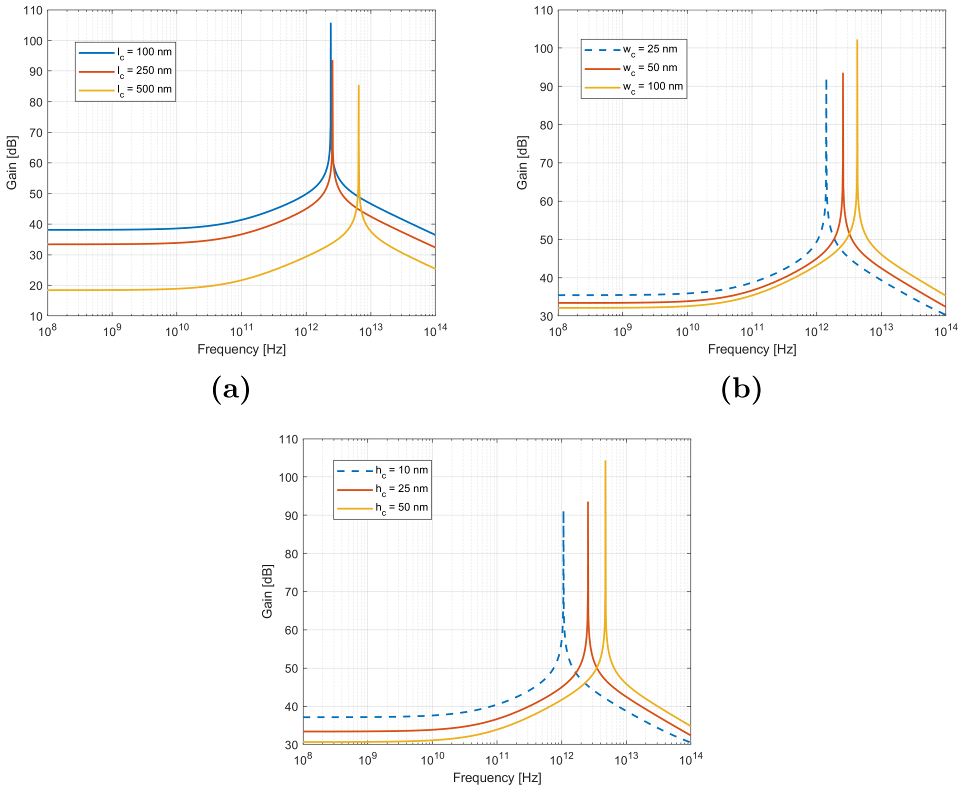

(c)

Figure 4.11: Dependence of the frequency behaviour on the geometry of the WSM channel.

Concerning the WSM channel, it is possible to notice how the dependence of the power gain on each dimension is monotonic: for increased dimension the power gain decreases. The good side effect is that the peak is shifted towards higher frequency, but in this trade-off we are obviously more interested in optimizing the power gain since the working frequency is already rather high. The dashed lines represent values that produce a current overshoot in the gate (i.e. it is not superconductive anymore) and therefore we need to select values bigger than that ones (or better, we need to optimize the length to section ratio).

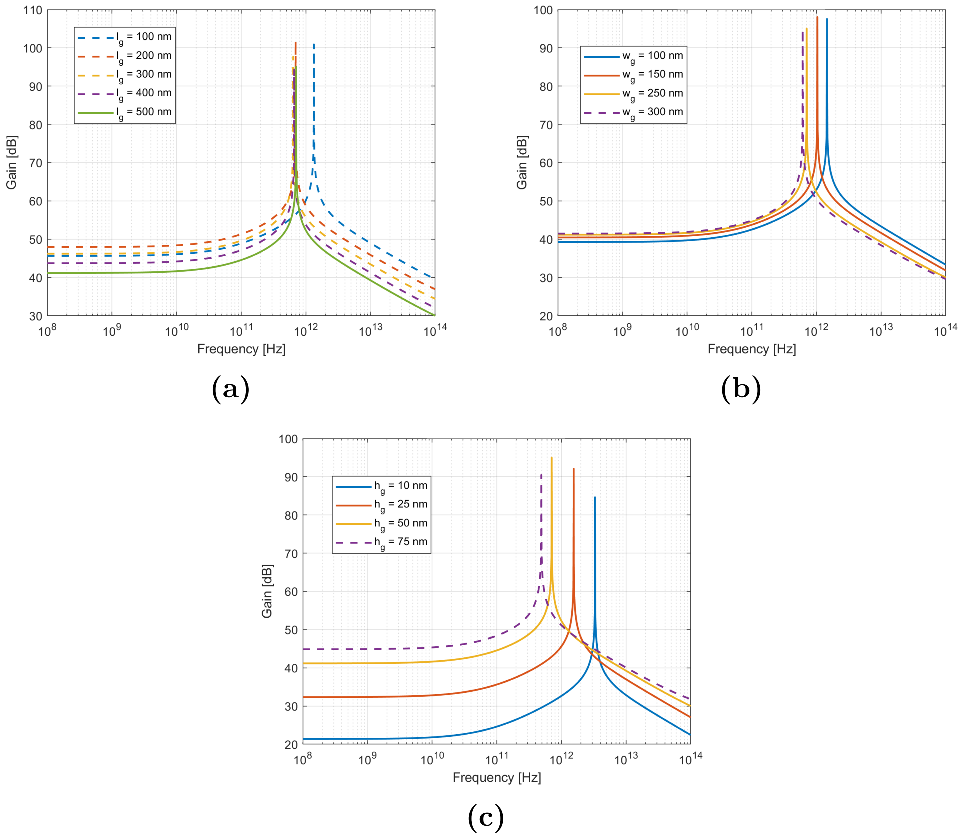

Figure 4.12: Dependence of the frequency behaviour on the geometry of the gate metal.

For the gate metal instead, it is possible to notice in Fig. 4.12a how the dependence is not monotonic: this is the only one of the analysed quantities that exhibits this kind of behaviour, thus proving the complexity of the relationships between the design of the device and its actual performance.

The oxide layer in principle is only needed to provide electrical insulation between the gate and the WSM channel. Since the gate-source capacitance depends on the characteristics of the oxide (permittivity and thickness), we want to minimize it by choosing a material which has a high permittivity and can be deposited in a thin film. The final choice is for a SiO_2 layer ($\epsilon_{SiO_2} = 3.9$) with a thickness of 5 nm (ALD is a possible solution for the oxide deposition).

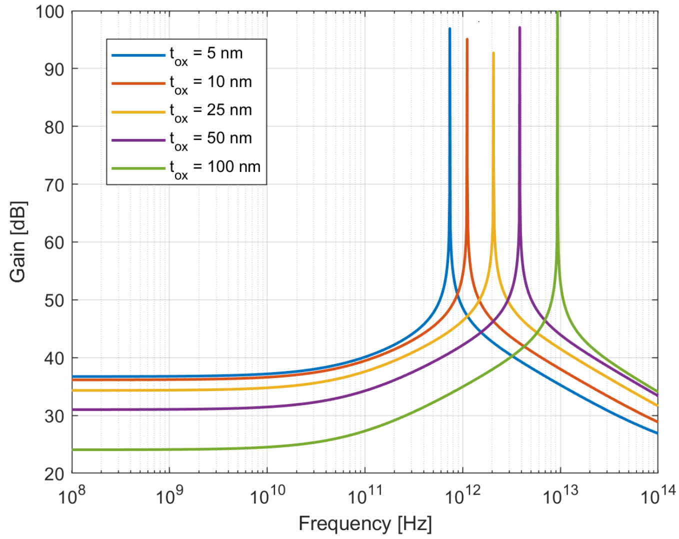

Figure 4.13: Frequency behaviour for different oxide thickness: it is possible to see how for smaller thickness (which means lower capacitance) the power gain is increased.

Lastly, in order to assume valid the 2D approximation for the solution of the London equation, we set an arbitrary condition that the WSM length should be at least two times its second biggest dimension (the width, in this case). This choice also grants the validity of another important assumption which is the fact that the magnetic field is negligible along the longitudinal direction (Eq. 4.2 holds only for the transverse MR).

Putting together the results of these analysis, a final device configuration is proposed (Tab. 4.2), with $V_G = 0.16\ mV$ and $V_{DS} = 50\ mV$. The corresponding frequency behaviour is shown in Fig. 4.14.

	Gate	WSM channel	Oxide layer
Length	300 nm	100 nm	100 nm
Width	150 nm	50 nm	50 nm
Height	60 nm	25 nm	5 nm

Table 4.2: Selected values for the final design of the device.

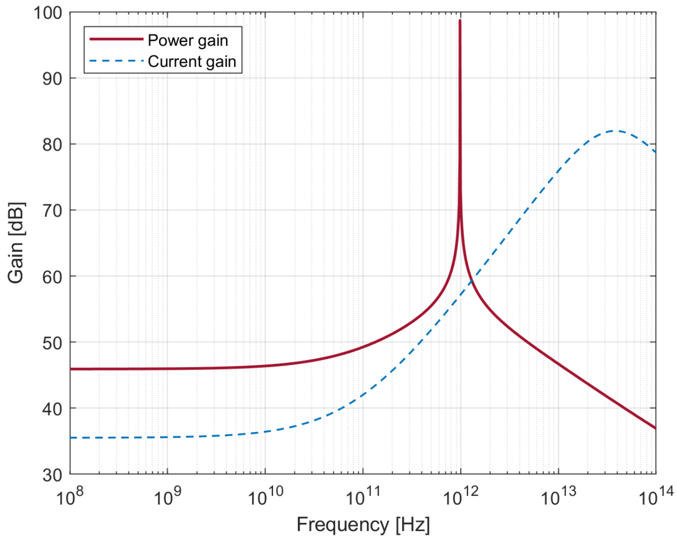

Figure 4.14: Frequency behaviour obtained with the design reported in Tab. 4.2; with $V_{DS} = 50\ mV$ and $V_G = 0.16\ mV$.

4.3.2 Stability

In order to further characterize the behaviour of the amplifier, the last figure of merit that was considered is the stability: an amplifier is unconditionally stable if a load or source can be connected without causing instability. For this condition to be true, the magnitudes of the reflection coefficients at the load, source and the input and output ports should be simultaneously less than one.

A practical way to test the stability of an amplifier is by means of the so-called Rollet factor, which is usually expressed in terms of the scattering parameters as follows:

$$K = \frac{1 - |S_{11}|^2 - |S_{22}|^2 + |\Delta|^2}{2\,|S_{12}S_{21}|} \tag{4.20}$$

Where:

$$\Delta = S_{11}S_{22} - S_{12}S_{21} \tag{4.21}$$

Since our device is characterized in terms of the Y parameters, we need to recall the relationship between the two formalisms, which is simply:

$$S = \frac{1 - Y}{1 + Y} \tag{4.22}$$

The amplifier is unconditionally stable if $K < 1$: by looking at Fig. 4.15 it is possible to notice how the condition is always achieved: however the increasing trend of the Rollet factor near the peak suggests that it probably would rise above the unit if all the high-frequency effects were considered in the model.

We can conclude that, by means of the Rollet factor, it is possible to establish that the proposed amplifier is unconditionally stable before the resonance peak, which is the actual range of interest of our device.

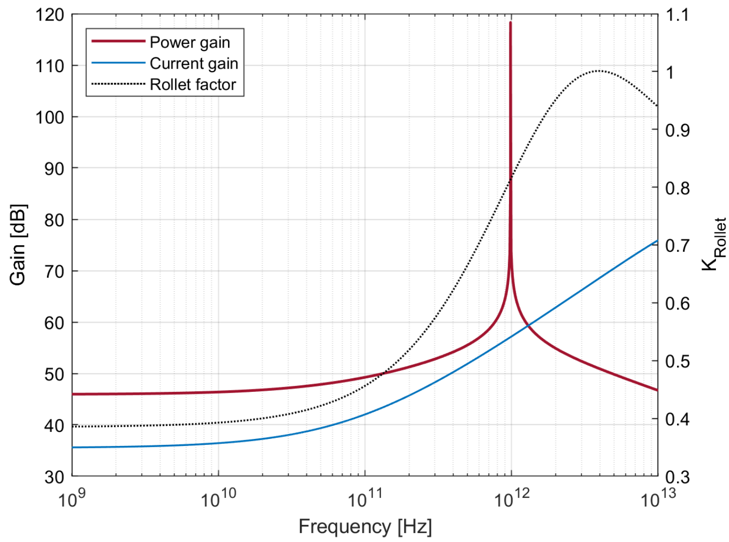

Figure 4.15: Frequency behaviour superposed with the Rollet factor: it is possible to see that the amplifier is definitely stable up to the Terahertz regime.

4.3.3 Competitive technologies

The actual state of the art solution for cryogenic amplification mostly consist of *High-electron-mobility transistors* (HEMT): as suggested by its name, the enhanced electron mobility is the key feature of this kind of transistors. The working principle relies on the formation of a 2DEG, which requires a heterostructure in order to from (a junction between a wide and narrow bandgap materials). Usually the selected materials are III-V compounds such as GaAs, AlGaAs, InP and so on. When the electrons arrive at the interface, they move from the wide bandgap material to the narrow one because of their tendency to occupy the lower energy states. A standard schematic of a HEMT is reported in Fig. 4.16.

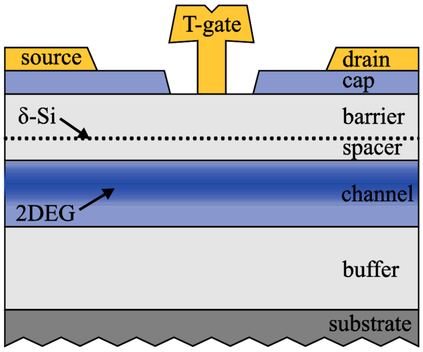

Figure 4.16: Schematic of a standard HEMT. Taken from [38].

The layer labeled as δ-Si is a doped sheet of Silicon, which is introduced to act as donors for the heterostructure, thus improving the electron density in the channel. Because the motion of the electrons in the channel is restricted to a quasi 2D plane, confined by two potential barriers, these electrons constitute the so-called two dimensional electron gas. The most important properties of the 2DEG are the number of electrons per unit area, referred to as sheet density, and the electronic mobility which is considerably higher than the one of standard electrons. The principle of operation follows the behavior of a field-effect transistor: an applied positive drain-source voltage is responsible for the lateral electric field which drives electron flow from the source to the drain. When a negative gate-source voltage is applied, the normal electric field due to the gate penetrates into the semiconductor and depletes the 2DEG underneath the gate contact, thus decreasing the drain-source current.

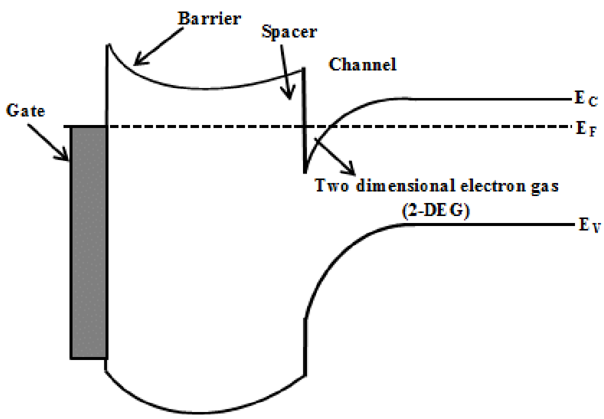

Figure 4.17: Graphical representation of the band diagram of a HEMT. Taken from [39].

HEMT are particularly indicated for cryogenic applications since they exhibits considerably high gain with low power consumption and consequently they can be placed near the emitting device (e.g. a qubit), at the coldest cryostat stage. This allows for a further reduction of parasitic capacitances and reduces the impact of environmental and thermal noise. In Fig. 4.18 is reported the frequency behaviour of an InP HEMT at different bias.

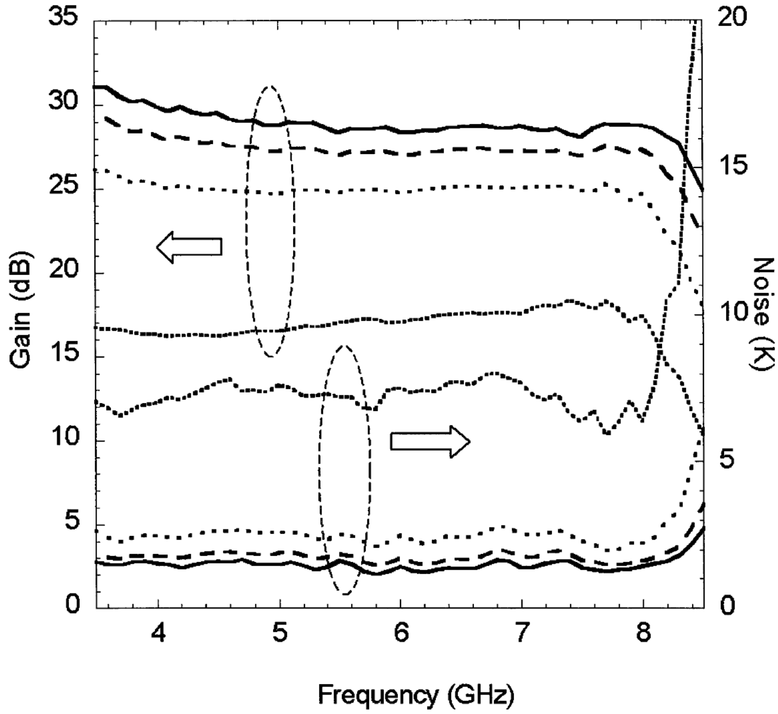

Figure 4.18: Measured results for an InP HEMT, at 14.8 K at different bias. From top to bottom: gain at bias point 1 (BP1), BP2, BP3, BP4, noise at BP4, BP3, BP2, and BP1. Corresponding bias points are shown in Tab. 4.3. Taken from [40].

	BP1	BP2	BP3	BP4
V_{DS} [V]	1.15	0.5	0.3	0.1
P_{DC} [mW]	11.5	3.0	1.0	0.1

Table 4.3: Bias points of the HEMT.

In order to have a clear comparison between the performances reported in Tab. 4.3 and the one of the proposed device, we evaluated the drain-source voltage and the DC power required to match the performance of BP1. The obtained results are reported in Tab. 4.4.

	V_{DS} [mV]	P_{DC} [μW]
WSA	10	3

Table 4.4: Drain-source voltage and power supply needed by the WSA to match the performances of BP1.

By comparing the two results we can appreciate how the WSM cryogenic amplifier is supposed to work significantly better than the HEMT counterpart since it requires a significantly lower power supply and it is able to exhibit comparable gain for a wider set of frequencies.

Future work includes experimental realization of an amplifier demonstrator, which will be able to confirm the results obtained in simulations: this will be strongly reliant on the access to epitaxial deposition of Weyl semimetal layers.

4.4 Perspectives and theoretical work

An experimental realization of the proposed device is yet to be achieved; nevertheless, also from the theoretical point of view there is room to improve both the understanding of the Weyl physics and the device model. A key aspect that has been already discussed, is the MR model of Weyl semimetal. At the present moment there is only a practical understanding of the MR behaviour of WSMs and consequently it is difficult to predict how the electronic transport mechanisms are changed for example when the device is scaled down (MR is a scattering-related mechanism, so what happens when the electronic mean free path is bigger than the device active length?).

4.4.1 Magnetoresistance modeling

The discovery of several material systems belonging to topological semimetals that exhibit extremely large magnetoresistance (up to two orders of magnitude higher than the magnetoresistance observed in metallic thin films [17]) has raised a fundamental question; whether this exceptional MR can be explained by classical magnetoresistance theories without considering the topological aspects or not. In fact, at the core of such exceptional magnetoresistance there is the peculiar band structure of three-dimensional topological semimetals that yields conducting surface states. Understanding the physical origin of this MR is crucial since in general, the study of electrical resistance is tightly related to the electronic transport mechanism. In this section it will be described the empirical model used in this work for characterizing the MR behaviour of the proposed WSA.

The material that is proposed in the WSA device is WP_2, which is a type-II WSM: this choice is motivated by the fact that, in these materials, the nearest Weyl points are of the same chirality, thus inducing robust surface states with exceptionally high mobility [16]. The zero-field resistivity of WP_2 is reported to exhibit a quasi-linear trend at high temperatures, where the electron-phonon scattering contribution is dominant. The low-temperature behaviour is more difficult to characterize since the transition to the saturation regime is narrower than what happens in classic metals (Fig. 4.19).

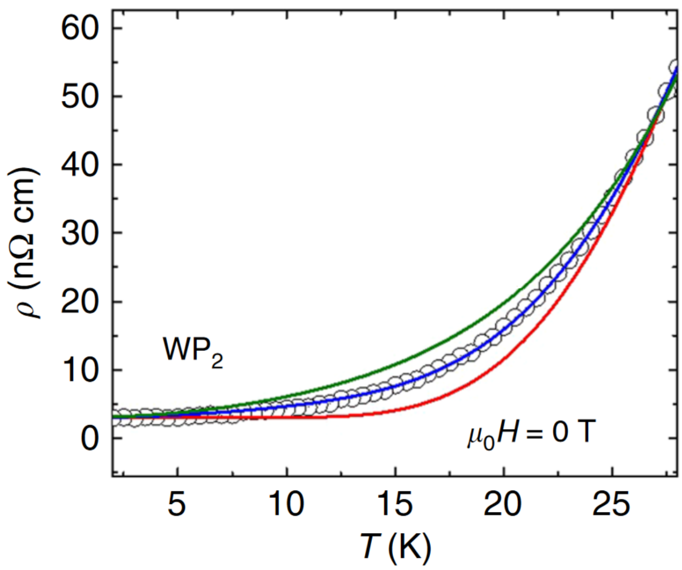

Figure 4.19: Low temperature resistivity of WP_2 at zero magnetic field, with different fitting curves. The best fit (blue solid line) takes into account three main mechanisms: electron-electron scattering, electron-phonon scattering and phonon drag[3]. Taken from [16].

By applying a magnetic field, the motion of electrons inside metals is obviously changed and consequently is the resistivity. In WP_2 we observe a huge magnetoresistance, despite a very high conductivity (Fig. 4.20).

[3]Phonon drag refers to an increase in the effective mass of electrons due to their interactions with the crystal lattice.

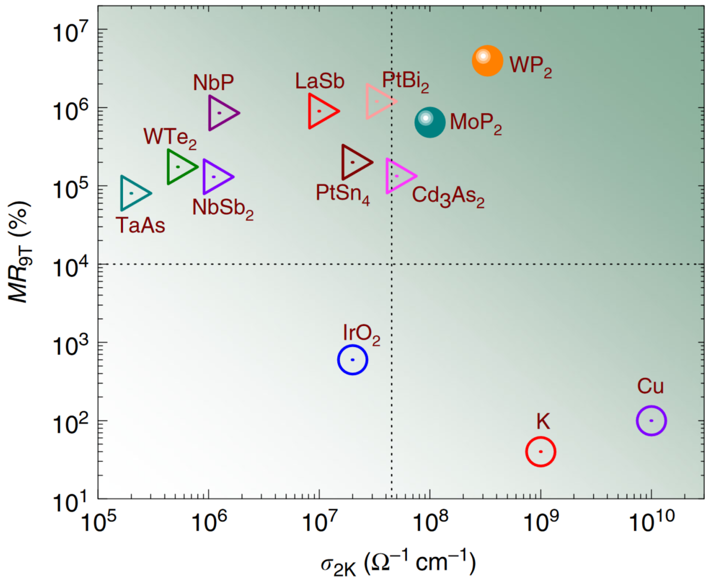

Figure 4.20: Comparison of MR and conductivity of some well-known metals and semimetals. The values of WP_2 and MoP_2 are evaluated at $T = 2\ K$ and $B = 9\ T$. Taken from [16].

Notice how the Weyl semimetals WP_2 and MoP_2 exhibit both a large conductivity and an extremely high magnetoresistance, which is unusual in standard metals.

The field dependence of the MR can be empirically expressed as reported in Eq. 4.2: this equation is used in order to fit the results obtained in [16] and to obtain the value of α which was used in the calculations (the power dependence of the resistivity on the applied field is reported to be quasi parabolic: in this work we set $m = 1.8$).

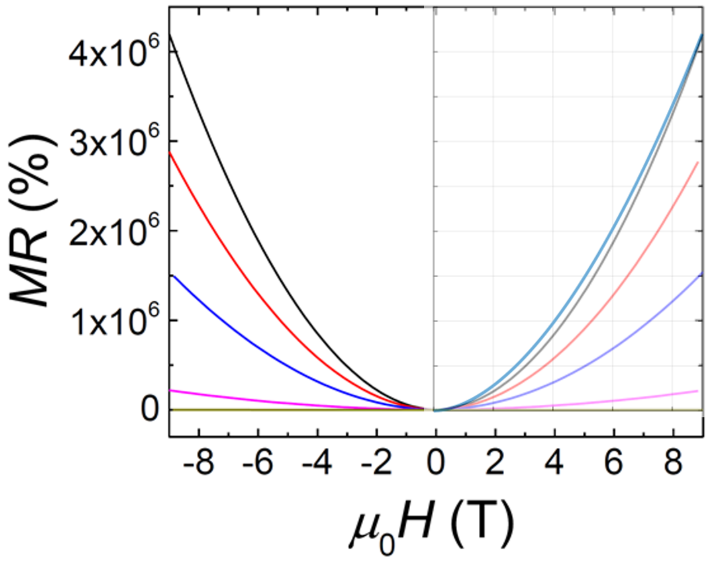

Figure 4.21: Fitted behaviour (blue line) of the experimental curve measured in [16]. The two results agree very well. The value of α which was used to obtain the fit is 41.14 $cm^2/V\ s$.

The fitted behaviour is the one at $T = 2\ K$, which seems a reasonable choice for the working temperature of the proposed device. Obviously, at different values of T, the MR behaviour is changed and therefore we would need different values of α.

In conclusion, also from the theoretical point of view, Weyl semimetal are still an open challenge. The model used for the simulations reported so far is able to provide exceptional results that motivate the pursuit of an actual realization of a Weyl semimetal amplifier, which can represent an ideal solution for quantum computers and in general for all kinds of cryogenic applications.

Chapter 5

Conclusions

The device simulations performed in this work have elucidated the potential of Weyl semimetals for novel electron devices.

In particular, the exotic trajectory exhibited by electrons in a WSM when subjected to crossed electric and magnetic field opens up the possibility for the realization of a new experimental setup for the detection of quantum oscillations. The possibility of having a simple and reliable method of identifying WSM phases in new materials is crucial in developing the understanding of these materials and offers the possibility of having a wider range of materials with different properties to be exploited for practical realizations. Moreover, further advances in the theoretical understanding of WSM transport phenomena can lead to the actual design of a high-frequency oscillator (up to the Terahertz regime), which promise to show high stability and field-dependent frequency control, together with the possibility of working well both at cryogenic and room temperature.

The proposed amplifier is in simulations able to operate with an extreme reduction of DC power, upwards to 100 times lower than standard HEMT technology, with comparable power gain, thanks to the negligible gate resistance provided by the superconductive gating and the enabling features of the magnetoresistive coupling offered by Weyl semimetals.

In general, the obtained results indicate that Weyl semimetals are highly promising for applications in cryogenic electronics, particularly those with highly strained power budgets such as quantum computing.

Appendix A

Derivation of the Weyl equation

The Weyl equation can be intended as a subset of the Dirac equation, which describes massless particles with half-integer spin (fermions). The Dirac equation can be obtained as a relativistic expansion of the Schrödinger equation, thus substituting the standard energy relationship (Eq. A.1) with the relativistic one (Eq. A.2).

$$E = \frac{p^2}{2m} \tag{A.1}$$

$$E^2 = m^2c^4 + c^2p^2 \tag{A.2}$$

By substituting Eq. A.2 in the Schrödinger equation one ends up with the so-called Klein-Gordon equation (Eq. A.3) which is indeed a relativistic Schrödinger equation, but unfortunately it does not include the particle spin.

$$-\hbar^2c^2\frac{\partial^2\Psi}{\partial t^2} = m^2c^4\Psi - \hbar^2c^2\Psi \tag{A.3}$$

In order to come up with a description that suits better the particles with spin, like electrons, Dirac proposed a sort of squared root of Eq. A.2, thus obtaining:

$$E = \beta mc^2 + c\alpha_j p_j \tag{A.4}$$

Where α_j and β are 4x4 matrices (Dirac matrices) that satisfy the following commutation relationships:

$$\begin{cases} \alpha_j\beta + \beta\alpha_j = 0 \\ \alpha_i\alpha_j + \alpha_j\alpha_i = 0 \\ \alpha_j^2 = \beta^2 = 1 \end{cases} \tag{A.5}$$

The α_j matrices can be expressed in terms of Pauli matrices as follows:

$$\alpha_j = \begin{bmatrix} 0 & \sigma_j \\ \sigma_i & 0 \end{bmatrix} \tag{A.6}$$

Similarly:

$$\beta = \begin{bmatrix} 1 & 0 \\ 0 & -1 \end{bmatrix} \tag{A.7}$$

By substituting Eq. A.4 in the Schrödinger equation, with some proper rearrangements, one ends up with the final Dirac equation:

$$(i\hbar\gamma^\mu\partial_\mu - mc)\psi = 0 \tag{A.8}$$

The last step required to obtain the Weyl equation is setting the mass to be equal to zero: notice that in this case the γ matrices[1] that were 4x4 in the Dirac formulation reduce to the Pauli matrices (2x2).

Here it is the Weyl equation:

$$\sigma^\mu\partial_\mu\psi = 0 \tag{A.9}$$

[1]In Eq. A.8, $\mu = 0,1,2,3$, with $\gamma^0 = \beta$ and $\gamma^j = \beta\alpha_j$.

Appendix B

Shot noise suppression in ballistic 1D devices

In 1918, Schottky reported that in an ideal vacuum tube (the ancestors of transistors) there were only two types of noise in the electrical current. The first type of noise is known as Johnson-Nyquist noise, or simply thermal noise. This kind of electronic noise is generated by the thermal agitation of the charge carriers inside an electrical conductor at equilibrium, which happens regardless of any applied voltage. The second type of noise is called shot noise and originates from the discrete nature of electric charge. If the electron transmission through a conductive system is fully uncorrelated, the shot noise can be modeled by a Poisson distribution. In nanosystems, shot noise can be suppressed as a result of correlations in the electron transmission imposed by the Pauli principle. In this appendix, it is reported a general expression of the power spectrum of noise, from which it is possible to show that, assuming the ballisticity of the considered system, the only source of noise is thermal noise.

In its general form, the noise power spectral density can be expressed as:

$$P(\omega) = 2 \int_{-\infty}^{\infty} dt \, e^{i\omega t} \langle \Delta I(t + t_0) \Delta I(t) \rangle \tag{B.1}$$

Where $\Delta I(t)$ represents the time-dependent fluctuations in the current at a given voltage and temperature. The brackets notation indicates an ensemble average over the initial time t_0.

If we plug in Eq. B.1 the well-known Landauer formula[1] for the quantized conductance, it is possible, with some manipulation, to obtain the following generalized expression:

$$P(\omega) = 4\pi\frac{q^2}{\hbar}\sum_{n=1}^{N}\left[2k_BT\,T_n^2 + T_n(1-T_n)qV\coth\Big(\frac{qV}{2k_BT}\Big)\right] \tag{B.2}$$

If there is complete transmission, i.e. the transmission probabilites T_n are equal to 1, the electrons are fully correlated and Eq. B.2 reduces to:

$$P(\omega) = 4\pi\frac{q^2}{\hbar}\sum_{n=1}^{N}2k_BT\,T_n \tag{B.3}$$

Since the Landauer conductance can be expressed as:

$$G = 2\pi\frac{q^2}{\hbar}\sum_{n=1}^{N}T_n \tag{B.4}$$

We recover the classical expression of thermal noise, which is in fact:

$$P_{th} = \frac{4k_BT}{R} \tag{B.5}$$

[1]The Landauer formula states that the conductance of a nanoscale material is given by the sum of all the transmission probabilities that an electron has when propagating with an energy equal to the chemical potential.

Bibliography

[1] J. Lorenzo Diaz-Cruz, Bryan Larios Lopez, O. Meza-Aldama, and Jonathan Reyes Perez. «Weyl spinors and the helicity formalism». In: (2015). arXiv: 1511.07477 [physics.gen-ph] (cit. on p. 2).

[2] Charles Day. «Takaaki Kajita and Arthur McDonald share 2015 Physics Nobel Prize». In: *Physics Today* (Oct. 2015). DOI: 10.1063/PT.5.7208 (cit. on p. 2).

[3] N.P. Armitage, E.J. Mele, and Ashvin Vishwanath. «Weyl and Dirac semimetals in three-dimensional solids». In: *Reviews of Modern Physics* 90.1 (Jan. 2018). ISSN: 1539-0756. DOI: 10.1103/revmodphys.90.015001 (cit. on pp. 2, 16).

[4] B. Q. Lv et al. «Experimental Discovery of Weyl Semimetal TaAs». In: *Physical Review X* 5.3 (July 2015). ISSN: 2160-3308. DOI: 10.1103/physrevx.5.031013 (cit. on pp. 2, 9).

[5] M.-Y. Yao et al. «Observation of Weyl Nodes in Robust Type-II Weyl Semimetal WP_2». In: *Physical Review Letters* 122.17 (May 2019). ISSN: 1079-7114. DOI: 10.1103/physrevlett.122.176402 (cit. on pp. 2, 10).

[6] Qian-Qian Yuan et al. «Quasiparticle interference evidence of the topological Fermi arc states in chiral fermionic semimetal CoSi». In: *Science Advances* 5.12 (2019). DOI: 10.1126/sciadv.aaw9485. eprint: https://advances.sciencemag.org/content/5/12/eaaw9485.full.pdf (cit. on p. 2).

[7] J. Jiang et al. «Signature of type-II Weyl semimetal phase in $MoTe_2$». In: *Nature Communications* 8 (2017). DOI: 10.1038/ncomms13973 (cit. on p. 2).

[8] Binghai Yan and Claudia Felser. «Topological Materials: Weyl Semimetals». In: *Annual Review of Condensed Matter Physics* 8.1 (2017), pp. 337–354. DOI: 10.1146/annurev-conmatphys-031016-025458 (cit. on pp. 3, 5, 6, 10, 18).

[9] Landau L. «The Theory of Phase Transitions». In: *Nature* (1936). DOI: 10.1038/138840a0 (cit. on p. 4).

[10] Mario Reis. *Chapter 11 - Landau Theory*. Ed. by Mario Reis. Boston: Academic Press, 2013, pp. 177–191. ISBN: 978-0-12-405545-2. DOI: https://doi.org/10.1016/B978-0-12-405545-2.00011-4 (cit. on p. 4).

[11] Joel E Moore. «The birth of topological insulators». In: *Nature* 464 (2010). DOI: 10.1038/nature08916 (cit. on p. 4).

[12] Chao-Kuei Lee et al. «Robustness of a Topologically Protected Surface State in a Sb_2Te_2Se Single Crystal». In: *Scientific Reports* 6 (2016). DOI: 10.1038/srep36538 (cit. on p. 5).

[13] Pavan Hosur and Xiaoliang Qi. «Recent developments in transport phenomena in Weyl semimetals». In: *Comptes Rendus Physique* 14.9 (2013). Topological insulators / Isolants topologiques, pp. 857–870. ISSN: 1631-0705. DOI: https://doi.org/10.1016/j.crhy.2013.10.010 (cit. on pp. 5, 7, 17–19).

[14] Shuo Wang, Ben-Chuan Lin, An-Qi Wang, Da-Peng Yu, and Zhi-Min Liao. «Quantum transport in Dirac and Weyl semimetals: a review». In: *Advances in Physics: X* 2.3 (2017), pp. 518–544. DOI: 10.1080/23746149.2017.1327329 (cit. on pp. 6–8).

[15] Liu, I., Heikes, C., Yildirim, and T. et al. «Quantum oscillations from networked topological interfaces in a Weyl semimetal». In: *npj Quantum Materials* 5 (2020). DOI: 10.1038/s41535-020-00264-8 (cit. on pp. 8, 9).

[16] Nitesh Kumar et al. «Extremely high magnetoresistance and conductivity in the type-II Weyl semimetals WP_2 and MoP_2». In: *Nature Communications* 8 (2017). DOI: 10.1038/s41467-017-01758-z (cit. on pp. 8, 42, 61–64).

[17] P Kumar, Sudesh, and S Patnaik. «Origin of exceptional magneto-resistance in Weyl semimetal $TaSb_2$». In: *Journal of Physics Communications* 3.11 (Nov. 2019), p. 115007. DOI: 10.1088/2399-6528/ab51a2 (cit. on pp. 9, 61).

[18] Andrew C. Potter, Itamar Kimchi, and Ashvin Vishwanath. «Quantum oscillations from surface Fermi arcs in Weyl and Dirac semimetals». In: *Nature Communications* 5.5161 (Oct. 2014). DOI: https://doi.org/10.1038/ncomms6161 (cit. on pp. 9, 20, 21, 29, 31, 37).

[19] Soluyanov, Alexey A., Dominik Gresch, Zhijun Wang, QuanSheng Wu, Matthias Troyer, Xi Dai, and B. Andrei Bernevig. «Type-II Weyl semimetals». In: *Nature* (2015). DOI: 10.1038/nature15768 (cit. on p. 10).

[20] M. Veldhorst, H. G. J. Eenink, C. H. Yang, and A. S. Dzurak. «Silicon CMOS architecture for a spin-based quantum computer». In: *Nature Communications* 8 (2017). DOI: 10.1038/s41467-017-01905-6 (cit. on pp. 11, 40).

[21] B. Patra et al. «Cryo-CMOS Circuits and Systems for Quantum Computing Applications». In: *IEEE Journal of Solid-State Circuits* 53.1 (2018), pp. 309–321 (cit. on p. 11).

[22] Paul Adrien Maurice Dirac and Ralph Howard Fowler. «The quantum theory of the electron». In: *Proceedings of the Royal Society of London. Series A, Containing Papers of a Mathematical and Physical Character* 117.778 (1928), pp. 610–624. DOI: 10.1098/rspa.1928.0023 (cit. on p. 14).

[23] Shengyuan A. Yang. «Dirac and Weyl Materials: Fundamental Aspects and Some Spintronics Applications». In: *SPIN* 06.02 (2016), p. 1640003. DOI: 10.1142/S2010324716400038 (cit. on p. 15).

[24] Ashok Das. *Lectures on Quantum Field Theory*. WORLD SCIENTIFIC, 2008. DOI: 10.1142/6938 (cit. on p. 15).

[25] Romilly Hills, Matej Brada, Y. Liu, Michael Pierpoint, M. Sobnack, W.M. Wu, and F. Kusmartsev. «From Graphene and Topological Insulators to Weyl Semimetals». In: (Jan. 2016), pp. 277–315. DOI: 10.1142/9789814740371_0012 (cit. on p. 16).

[26] Ilya Belopolski et al. «Criteria for Directly Detecting Topological Fermi Arcs in Weyl Semimetals». In: *Phys. Rev. Lett.* 116 (6 Feb. 2016), p. 066802. DOI: 10.1103/PhysRevLett.116.066802 (cit. on p. 17).

[27] H.B. Nielsen and M. Ninomiya. «Absence of neutrinos on a lattice: (I). Proof by homotopy theory». In: *Nuclear Physics B* 185.1 (1981), pp. 20–40. ISSN: 0550-3213. DOI: https://doi.org/10.1016/0550-3213(81)90361-8 (cit. on p. 18).

[28] Peng Li et al. «Evidence for topological type-II Weyl semimetal WTe_2». In: *Nature Communications* 8 (2017). DOI: 10.1038/s41467-017-02237-1 (cit. on p. 20).

[29] K. Saermark, J. Lebech, and H. Johansen. «On the concept of cyclotron resonance in metals». In: *physica status solidi (b)* 83.1 (1977), pp. 187–195. DOI: 10.1002/pssb.2220830121 (cit. on p. 22).

[30] Haibo Yao, Mingfeng Zhu, Liwei Jiang, and Yisong Zheng. «Simulation on the electronic wave packet cyclotron motion in a Weyl semimetal slab». In: *Journal of Physics: Condensed Matter* 29.15 (Mar. 2017), p. 155502. DOI: 10.1088/1361-648x/aa5f94 (cit. on pp. 22, 25–27, 38).

[31] Song-Bo Zhang, Hai-Zhou Lu, and Shun-Qing Shen. «Linear magnetoconductivity in an intrinsic topological Weyl semimetal». In: *New Journal of Physics* 18.5 (May 2016), p. 053039. DOI: 10.1088/1367-2630/18/5/053039 (cit. on pp. 24, 25).

[32] J. Hu, Y. L. Zhu, D. Graf, Z. J. Tang, J. Y. Liu, and Z. Q. Mao. «Quantum oscillation studies of the topological semimetal candidate ZrGeM(M=S,Se,Te)». In: *Physical Review B* 95.20 (May 2017). ISSN: 2469-9969. DOI: 10.1103/physrevb.95.205134 (cit. on p. 35).

[33] Yi Zhang, Daniel Bulmash, Pavan Hosur, Andrew C. Potter, and Ashvin Vishwanath. «Quantum oscillations from generic surface Fermi arcs and bulk chiral modes in Weyl semimetals». In: *Scientific Reports* 6 (2016). DOI: `10.1038/srep23741` (cit. on p. 37).

[34] Aifeng Wang, D. Graf, Yu Liu, Qianheng Du, Jiabao Zheng, Hechang Lei, and C. Petrovic. «Large magnetoresistance in the type-II Weyl semimetal WP_2». In: *Physical Review B* 96.12 (Sept. 2017). ISSN: 2469-9969. DOI: `10.1103/physrevb.96.121107` (cit. on p. 42).

[35] Victor Corchete. «Superconductors - the Meissner effect - the London equation». In: (Oct. 2019) (cit. on p. 42).

[36] B. W. Maxfield and W. L. McLean. «Superconducting Penetration Depth of Niobium». In: *Phys. Rev.* 139 (5A Aug. 1965), A1515–A1522. DOI: `10.1103/PhysRev.139.A1515` (cit. on p. 43).

[37] A. Toniato, B. Gotsmann, E. Lind, and C. B. Zota. «Weyl Semi-Metal-Based High-Frequency Amplifiers». In: *2019 IEEE International Electron Devices Meeting (IEDM)* (Dec. 2019), pp. 9.4.1–9.4.4. ISSN: 2156-017X. DOI: `10.1109/IEDM19573.2019.8993575` (cit. on p. 45).

[38] Andreas R. Alt. «Ultra-low noise InP HEMTs for cryogenic applications». In: *ETH Doctoral Thesis* (2013). DOI: `https://doi.org/10.3929/ethz-a-009781835` (cit. on p. 58).

[39] Supriya and Sweety. «Ballistic Mobility Degradation Effect in 25 nm Single Gate HEMT». In: *Nanocon 012 - II international conference on Nanotechnology Innovative materials, Processes, Product and Materials* (Oct. 2012) (cit. on p. 58).

[40] N. Wadefalk et al. «Cryogenic wide-band ultra-low-noise IF amplifiers operating at ultra-low DC power». In: *IEEE Transactions on Microwave Theory and Techniques* 51.6 (2003), pp. 1705–1711. DOI: `10.1109/TMTT.2003.812570` (cit. on p. 59).